



A review of advances in resistance spot welding of automotive sheet steels: emerging methods to improve joint mechanical performance

Imtiaz Ali Soomro^{1,2} · Srinivasa Rao Pedapati¹ · Mokhtar Awang¹

Received: 17 May 2021 / Accepted: 2 September 2021 / Published online: 22 September 2021
© The Author(s), under exclusive licence to Springer-Verlag London Ltd., part of Springer Nature 2021

Abstract

The use of resistance spot welding (RSW) in the automotive industry is by far the most preferred and widely used joining technique for sheet metal parts and is likely to continue for the foreseeable future. Advanced high strength steels (AHSSs) are most commonly used in automotive structural components due to their attractive strength-ductility combinations. However, several challenges are faced during RSW including (1) complex phase transformations such as hardening of nugget due to brittle martensitic structure and softening in the heat affected zone due to martensite tempering present in base metal, cast like solidification structure of nugget (2) elemental segregation leading to grain boundary embrittlement, (3) solidification defects such as porosity and void formation in nugget, and (4) liquid metal embrittlement cracking. All of above factors contributes in degradation of joint mechanical properties. In recent years, interlayer assisted RSW, magnetically assisted RSW, and pulsed-RSW have emerged as potential methods to improve the joint mechanical performance. This review paper seeks to summarize the recent technological advances of three modified RSW processes. A comprehensive analysis of the effect of welding process parameters on metallurgical features of the weld joint, mechanical performance, and failure behaviour under different loading conditions, i.e. cross tension, tensile shear, and cyclic (i.e. fatigue), is presented. In addition, the process feasibility to various AHSS grades is also discussed. Finally, current challenges and new opportunities arising from three modified RSW processes are discussed to provide a basis for future research.

Keywords Advanced high strength steels · Resistance spot welding · Cross tension test · Tensile shear test · Interfacial failure mode

1 Introduction

Over the past few years, automotive industry is saddled with the increasing demand to reduce tailpipe emissions and to improve the vehicle fuel efficiency. Vehicle weight reduction is considered as one of the effective ways to improve fuel economy [1–3]. About 60% of a vehicle's weight consists of

body and chassis components [4]. Reducing the body component thickness can substantially lower the vehicle weight. However, a large reduction in component thickness can be detrimental to vehicle crashworthiness (defined as ability of vehicle structure to absorb energy during collision) which is of paramount importance with regard to passenger safety [5].

Weight reduction and safety are contradictory challenges as improved safety is generally provided by increased component thickness which in turn increased the weight [3, 5]. Apart from that, automobile body structure requires high structural static stiffness, durability, noise vibration and harshness (NVH) control, and ease of manufacturability to be formed into complex shapes [6]. Auto manufacturers are searching for light materials that help them to fulfil the diverse requirements of emissions, efficiency, safety, manufacturability, and durability at a relatively low cost. Many new materials such magnesium alloys, aluminium alloys, and polymer matrix composites have been developed but none of them have shown the versatility of steel [1, 4]. Steel is the time-tested material. It

✉ Imtiaz Ali Soomro
imtiaz_17007503@utp.edu.my

¹ Department of Mechanical Engineering, Universiti Teknologi PETRONAS, 32610 Seri Iskandar, Perak, Darul Ridzuan, Malaysia

² Department of Metallurgy and Materials Engineering, Mehran University of Engineering and Technology, Jamshoro, Sindh 76062, Pakistan

has been used for generations as material of preference for automotive applications. Its unique processing capabilities and metallurgical properties make it able to keep pace with auto industry requirements [1, 7].

There is a wide range of steels available to the automotive designer for use in modern vehicle architectures. Among them, advanced high strength steels are the primary material used for automobile body structures [6, 8–11]. These steels provide a variety of strength and ductility levels that helps auto manufacturers to down-gauge the part thickness to reduce the mass of vehicles while maintaining vehicle safety, thereby increasing fuel economy and reducing tailpipe emissions [6, 12]. Figure 1 shows a diagram that relates the elongation to the strength of AHSSs with the conventional high strength steels (HSS). The family of AHSSs includes first-generation transformation-induced plasticity (TRIP) steel, dual phase (DP) steel, complex phase (CP) steel, martensitic steel (MS), and press-hardened (PH) steel [9, 14, 15]. Second generation mainly comprise TWIP steel (twin-induced plasticity), L-IP steel (lightweight with induced plasticity), austenitic stainless steel (AUST.SS), and SIP steels (shear band formation-induced plasticity) [8, 11, 16]. The first- and second-generation AHSSs are widely used in vehicle body in white (BIW) parts such as A, B, and C pillars due to their high tensile strength, good formability, and capacity for high energy absorption [5, 6, 17]. Third-generation AHSS grades are currently undergoing research. However, some grades such as quenching and partitioning (Q&P) steel [9, 18, 19] and TRIP steel with medium to high Mn content [13, 20] are developed with a better combination of strength and ductility than the first- and second-generation ones at lower production cost.

1.1 Resistance spot welding

RSW process was firstly invented by Elihu Thomson in 1877 [21]. The use of RSW in vehicle manufacturing dates back to 1930s and is by far the most preferred and widely used in

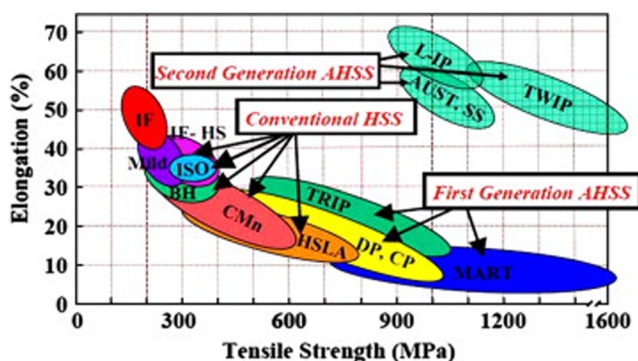


Fig. 1 The strength versus elongation relationship for conventional HSSs and [13]

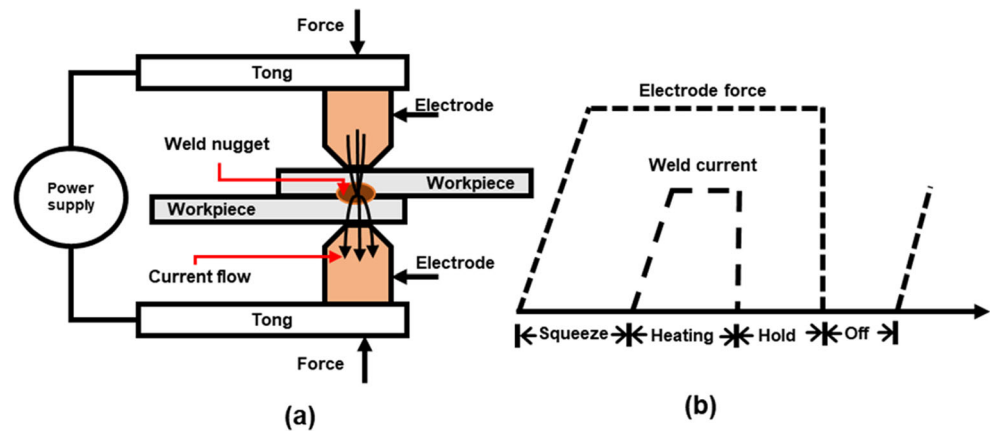
automotive body assembly line. In RSW process, large current flows through the stack of sheet metals to be joined. The high contact resistance at the faying surfaces generates heat, causing localized melting and subsequent coalescence of a small volume of material, forming the weld nugget [22–24]. A schematic of RSW process is shown in Figure 2a. In RSW process, the required process heat is generated by Joule heating, which is governed by the following equation:

$$Q = I^2 R t \quad (1)$$

where Q (J) is the heat generated, I (A) is the applied current, R (Ω) is the total resistance (i.e. contact plus bulk resistances) across the electrodes, and t (s) is the welding time [21, 25–27]. In RSW process, a weld nugget starts to form when sufficient heat has been put at the faying interface to begin the formation of a molten weld pool. After cooling, an elliptical-shaped nugget is formed keeping the sheets together [28, 29]. RSW process involves the simultaneous application of sufficient force and high electrical current over a short time to keep molten material inside the weld nugget. The force and welding current are applied via water-cooled copper alloy electrodes [22, 30]. The electrode force, welding current, welding time, and resistance of workpieces influence the heat input which in turn determines the size of the formed nugget. The excessive heat input can lead to expulsion of liquid metal from the nugget, whereas low heat input may result in insufficient melting [31, 32]. A typical RSW process consists of four distinct stages, as shown in Figure 1b. Stage 1 comprise of pressing of the work pieces by the electrodes to brought in contact the surface of the sheets, stage 2 involves heat generation at the faying interface due to resistance to flow of current, stage 3 consists removal of current while pressure is maintained to permit the solidification of the melted zone, and the stage 4 accounts for release of electrode from the workpieces [33].

RSW is an autogenous welding process; hence, no filler material is required to create a joint [31, 34, 35]. Ease of automation, high compatibility with steel sheets, light weight, and stable performance make RSW economically viable joining process for mass production [31, 36, 37]. Several thousand spot weld joint are made in a typical modern vehicle body [38–41], and 75% of the body assembly workload is carried by these joints [37]. Spot welds failure can influence the stiffness and NVH performance of the vehicle [40]. Further, spot welds act as fold initiation site to manage impact energy to transfer loads through the vehicle's frame during crash event [42]. To ensure the passenger safety in crash event, the integrity of the component should be kept intact at maximum extent. Therefore, the performance of spot welds can affect crashworthiness and structural integrity of the vehicle [41, 43–45].

Fig. 2 **a** Schematic illustration of RSW and **b** stages of typical RSW cycle



Based on previous research survey, it is recognized that AHSSs face a number of challenges during RSW, including the following:

1.1.1 Complex phase transformation and embrittlement of weld joint

- The strength and ductility of AHSSs are controlled by their multi-phase microstructures, which are carefully designed. The desired microstructures with the appropriate volume, size, and distribution of phases are created using a combination of alloying elements and thermo-mechanical treatment. The increased alloying content required to increase the strength of these materials results in high hardenability. [46]. Further, RSW process involves high cooling rates roughly in order of 3000 K s^{-1} for 2.0-mm sheet thickness to over 10^5 K s^{-1} for sheet thicknesses less than 0.5 mm [47, 48]. Rapid cooling rates inherent in RSW coupled with high hardenability results in the typically martensitic structure in the fusion zone (FZ) and heat affected zone (HAZ) of AHSS weld. This hardened microstructure in the weld causes interfacial fracture during high strain rates encountered in impact conditions, such as in event of vehicle collision, which is undesirable due to low elongation and energy absorption. [38, 46, 47, 49–53]. Moreover, softening occurs in subcritical heat affected zone (SCHA) during the welding of AHSS-containing martensite (e.g. dual phase steels, martensitic steels, hot stamped boron steel) [53–62] which degrades the weld mechanical properties.
- Furthermore, nowadays duplex stainless steels (DSSs) are recognized as excellent candidates for structural applications in the automotive industry due to their combination of superior mechanical properties and high corrosion resistance [63]. The key issue with DSSs is the formation of an unbalanced austenite/ferrite microstructure in the fusion zone (FZ) during RSW. A fully ferritic structure is formed in FZ of DSS weld at the end of solidification

along with precipitation of Cr_2N particles. The ferritization of the FZ and formation of Cr_2N particles degrades the fracture toughness and reduce corrosion resistance of the welds [63–65].

- In general, microstructure of FZ of resistance spot welds consists of large columnar/dendritic grains. These columnar/dendritic grains are oriented along the direction of heat flow and are perpendicular to fusion line. It has been reported that large columnar grains have low fracture toughness and provide weak interface along the fusion line, thus ease the crack propagation through FZ and the resultant weld joint fail in brittle interfacial failure (IF) mode [52, 66]. Generally, failure of resistance spot weld occurs in two modes, i.e. (i) IF mode and (ii) pullout failure (PF) mode. In PF mode, failure occurs via complete (or partial) nugget withdrawal from one sheet. In IF mode, failure occurs via crack propagation through fusion zone. Failure mode significantly affects the energy absorption and load bearing capacity of spot welds. Vehicle crash-worthiness is significantly reduced when spot welds fail via the IF mode [67].

1.1.2 Elemental segregation, solidification defects, and liquid metal embrittlement

- In AHSS resistance spot welds, alloying elements like phosphorous, sulphur, and manganese tend to segregate to the grain boundaries mainly at weld nugget edge [68, 69]. In addition, complex nonmetallic inclusions are also formed in the FZ [68]. These both factors reduce the fracture toughness of weld nugget and promote susceptibility to IF mode. Furthermore, rapid cooling rates associated with RSW process increase the tendency towards solidification cracking, voids, and porosity formation in FZ which can add to the chances of IF mode of AHSS weld [31, 70–72].

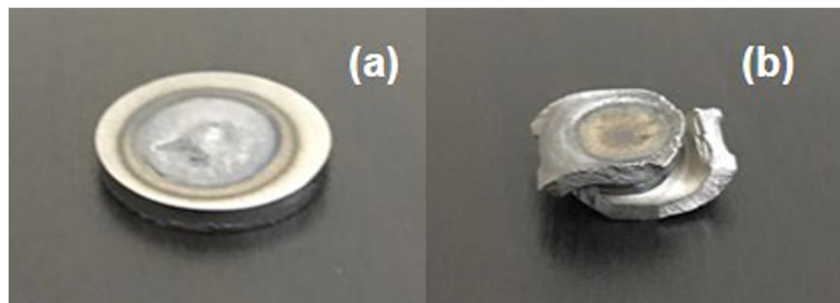
- To prevent corrosion, a large percentage of automotive steels are produced in the form of galvanized and galvanized products [73]. Liquid metal embrittlement (LME) of spot weld is another grave issue which arise during RSW of Zn coated AHSSs. LME cause cracks in the surface of the weld and can have detrimental effect on mechanical performance of welded joint. LME occurs due to the penetration of the liquid zinc along grain boundaries during RSW [74–79].

To improve the quality and performance of AHSS resistance spot welds, a proper approach is required to obtain pull-out failure mode. Figure 3 shows the typical IF mode and PF mode observed in RSW joint. In a crash, the PF mode induces extreme plastic deformation in adjacent components and increases strain energy dissipation. Since the amount of energy absorb by the weld is greater in the PF mode, thus it is usually preferred over IF mode [43, 80, 81].

Generally, enlarging the nugget diameter is considered as the most convenient way of ensuring PF mode in a resistance spot weld [82]. The joint strength also improves as the nugget diameter grows. The strengthening is achieved due to the fact that increasing the nugget diameter reduces the stress concentration on the nugget edge, impeding crack initiation and propagation [83]. Some industrial standards such as AWS/ANSI/AISI [84] recommended a minimum weld size based on $D = 4t^{0.5}$ (where D is weld nugget diameter and t is sheet thickness) criterion, while Japanese standard JIS Z3140 [85] and German standard DVS2923 [86] recommended a minimum weld size based on $D = 5t^{0.5}$ criterion to ensure PF mode in resistance spot welds of automotive steels. Although these standards work well for conventional low carbon steels; however, standard merely based on the sheet thickness does not guarantee PF mode in AHSS weld [36, 40, 87]. This is because these standards assume homogenous mechanical properties across the weldment and do not consider the effect of metallurgical, i.e. hardening of FZ and softening of HAZ that can significantly affect the failure mode. Pouranvari et al. [88, 89] proposed an analytical model for the occurrence of PF mode in AHSS weld given as

$$D_c = \frac{4t}{Pf} \frac{H_{PFL}}{H_{FZ}} \quad (2)$$

Fig. 3 Typical failure modes observed in spot weld: **a** IF mode and **b** PF mode



where D_c is minimum FZ size, P is the porosity factor, t is sheet thickness, f is the ratio of shear strength to tensile strength of the FZ, and H_{PFL} and H_{FZ} are hardness of the FZ and PF location, respectively. According to the model, spot weld with $D > D_c$ will fail in the PF mode and spot weld with $D < D_c$ will fail in IF mode during tensile shear (TS) test. Spot welds that failed in the PF mode during the tensile shear test are also likely to fail in the PF mode during the cross tension (CT) test and peel test [22]. In practice, it is likely to be more difficult to maintain consistently large weld nugget size in production. Larger weld nugget sizes require higher welding current that causes higher heat input, which increases the susceptibility to expulsion [90]. Moreover, AHSS requires higher electrode force compare to low carbon steel during RSW. Higher heat input along with higher electrode force may also increase the depth of indentation at weld surface [80, 90]. Indentation and notch at the nugget edge are other factors that significantly affect failure mode [43, 91]. A deep indent reduces the effective nugget area while a sharp notch act as stress concentration point which promotes interfacial fracture of the weld. In summary, failure behaviour and mechanical properties of AHSS resistance spot weld depend on complex interplay between weld geometrical factors (i.e. nugget size, shrinkage void, porosity, notch shape, and indentation depth), weld metallurgical features (i.e. microstructure of BM, HAZ, and FZ), and stress state (i.e. tensile shear, cross tension, and coach peel loading) [53].

Three potential approaches in literature have been reported to resolve the challenges regarding transition of IF mode to PF mode and to improve the mechanical performance of RSW joint namely (1) interlayer assisted RSW (IA-RSW), (2) magnetically assisted RSW (MA-RSW), and (3) pulsed RSW. In this review, the advances in three methods are reviewed with focus on AHSSs welding.

2 Interlayer-assisted RSW

In IA-RSW, a transition material such as foil/shim/sheet/coating is placed between workpieces to modify the chemical composition/microstructure of weld nugget which improves the mechanical performance of the joint. This approach is

either used to produce a tough microstructure in the FZ via dilution process [92] or to control the composition of intermetallic compounds (IMCs) at the interface in dissimilar steel/X alloy joint (where X can be Al, Mg, Ti, etc) [93–98]. Figure 4 shows the schematic of IA-RSW. Different types of interlayer materials are used to improve the weldability of various similar and dissimilar alloy combination. The selection of interlayer material depends upon chemistry, melting point, solid solubility in base metal, electrical and thermal conductivity, and other physical and metallurgical factors [99]. In this review, focus has been given to IA-RSW of similar and dissimilar steels. Table 1 compares the peak load and failure mode of conventional RSW weld and IA-RSW weld of different automotive steels.

Aghajani and Pouranvari [92] investigated the effect of a 0.5-mm-thick nickel interlayer on joint microstructure and mechanical performance of 1.5-mm-thick sheets of AISI420 martensitic stainless steel (MSS) resistance spot weld. Results showed that the addition of interlayer increased Ni content from 0.09% in BM to 21.3% in FZ of MSS/Ni/MSS joint. It was found that MSS/MSS weld failed in IF mode due to brittle martensite formation along with some δ -ferrite in FZ during TS and CT tests. On the other hand, MSS/Ni/MSS weld failed in PF mode during both types of tests (refer to Figure 5) due to the formation of complete austenite structure embedded with Cr-rich carbides. The addition of Ni interlayer lowers the FZ hardness and improved peak load and energy absorption under both loading conditions. The IF to PF mode transition was attributed to austenitic structure due to dilution of weld nugget with the addition of Ni interlayer.

Li et al. [20] used a 0.8-mm-thick uncoated IF steel shim to make RSW joint in uncoated medium-Mn TRIP steel. They used two schemes to place IF steel shim, i.e. (1) at the faying

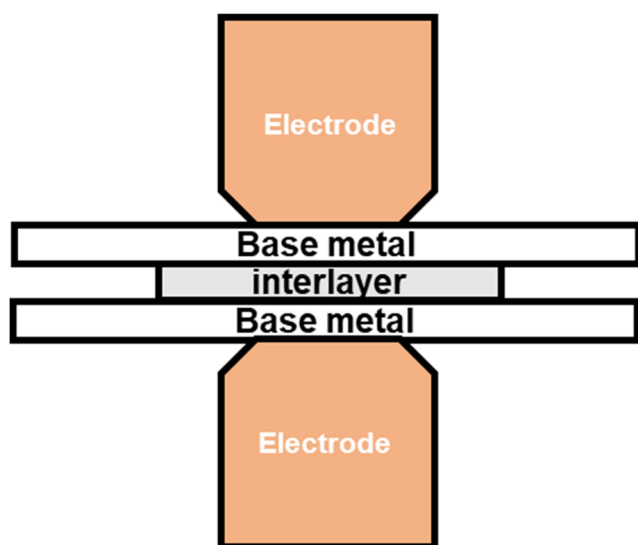


Fig. 4 Schematic of IA-RSW process

interface (shim-in) and (ii) against the electrodes (shim-out). Results showed that mixing of ultra-low carbon IF steel (i.e. shim-in) results in dilution of liquid metal in weld nugget which subsequently lowers the carbon and manganese content of FZ. Although the microhardness of FZ decreased in shim-in specimen, however, addition of IF steel (either shim-in or shim-out) did not show any effect on FZ microstructure and brittle martensite phase still dominated in FZ. Under TS and CT loading, the best mechanical properties in terms of peak load and energy absorption were observed in shim-out specimen due to higher weld nugget size and expulsion free weld compared to shim-in and shim-free welds (refer to Figure 6).

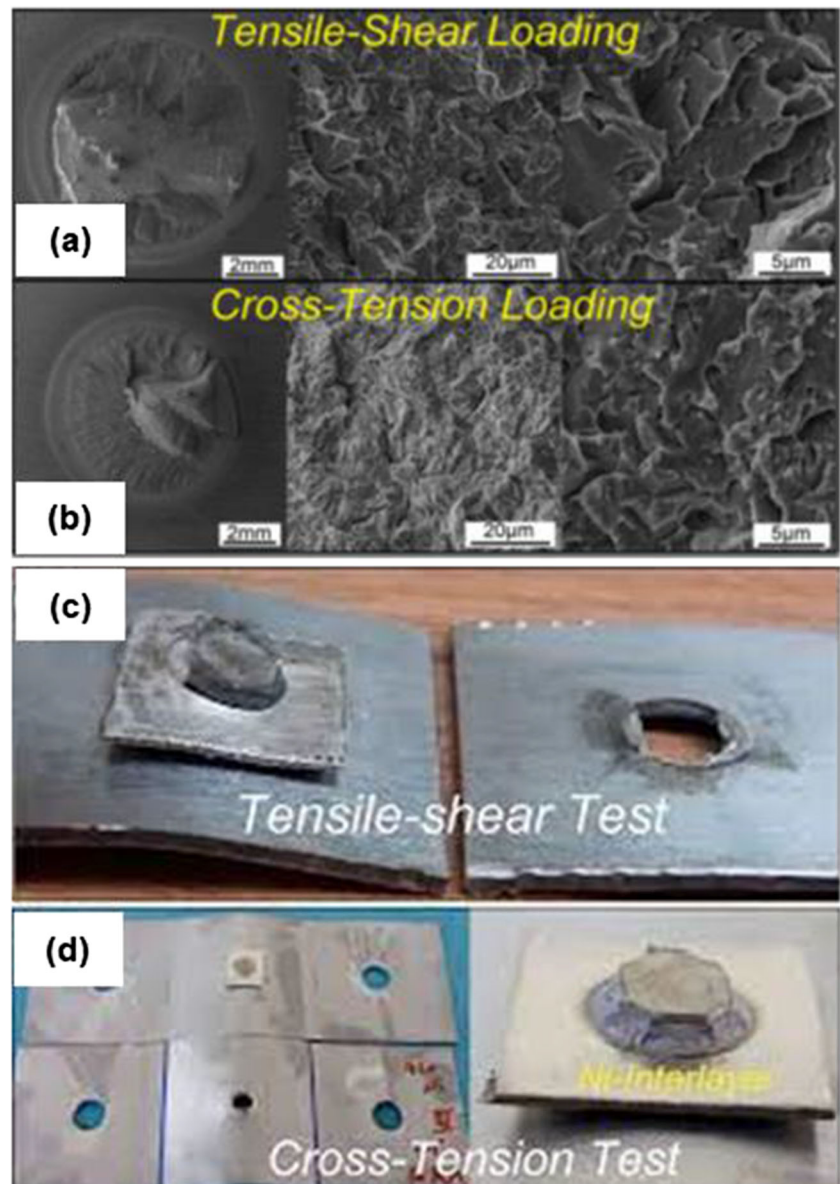
On contrary, Peterson [103] showed that inserting a low carbon steel shim between the high carbon equivalent steel sheets can lower the carbon content and hardness of the FZ via dilution process promoting the PF mode. Das et al. [101] added graphene nanoplatelets (GNPs) as interlayer at AISI 1008 steel resistance spot weld interface. It was found that TS peak load and failure energy of GNP coated weld is significantly enhanced compared to the traditional RSW weld. The improvement in mechanical properties was attributed to formation Fe-GNP nanocomposite in weld nugget in which GNPs strengthening the Fe matrix.

Mookam [100] found that introducing 1-mm-thick Ag alloy interlayer at the interface of DP590 steel/AISI 304 ASS steel dissimilar RSW weld resulted in improved tensile strength compared with interlayer free weld. However, the interlayer assisted weld failed in IF mode. Microstructure and EDS analysis showed that the weld interface was composed of three IMC layers, as shown in Figure 7. Layer A is composed of $Ag_{0.4}Fe_{0.6}$ phase, layer B is a Cu-rich phase, and layer C is Cu-rich phase surrounded by fine grain boundaries of $Ag_{0.4}Fe_{0.6}$. The improvement in mechanical performance of interlayer assisted weld was attributed to the formation of IMCs in weld interface.

He et al. [76] investigated the effect of an aluminium interlayer on LME suppression in TRIP1100 and TRIP1200 steel grades. Aluminium foil of 25- μ m thickness were added between the electrode/steel interface. They found that the average LME crack length for TRIP1100 decreased by 70%, while for TRIP1200 decreased by 30% with addition of aluminium interlayer. Moreover, a full tensile shear strength recovery for TRIP1100 while a 90% tensile shear strength recovery for TRIP1200 was claimed with the use of aluminium interlayers. They also found that addition of aluminium interlayers resulted in the formation of iron-aluminides of types as $FeAl$, $FeAl_2$, and Fe_2Al_5 that impede liquid zinc from contacting the steel surface, thus preventing LME. However, the large difference in melting point between steel and aluminium and the formation of Fe-Al IMCs raises concerns about the reliability of using Al interlayers to mitigate LME.

Table 1 Comparison of peak load and failure mode between RSW weld and IA-RSW weld of different grades of steel

RSW			IA-RSW			
Work piece material/ thickness	Failure mode	Peak load (kN)	Interlayer material/thickness	Peak load (kN)/improvement compared to RSW	Failure mode	Ref
AISI420 MSS/1.5 mm	IF ^{a,b}	Ni/0.5 mm	Improved by factor of 1.4 ^a and 4.2 ^b	PF ^{a,b}	[92]
DP590 steel//AISI 304 ASS 1.2/1.2 mm	IF ^a	Ag alloy/1.0 mm	Improved by 23.07% ^a	IF ^a	[100]
AISI 1008 steel/0.6 mm	IF ^a	Graphene nano platelets (GNP)/94 μm	Improved by 64% ^a	PF ^a	[101]
Medium Mn TRIP steel/1.4 mm	IF ^{a,b}	16 ^a 2 ^b	Interstitial free steel/0.8 mm	12 ^a 3 ^b (shim in method)	PF ^{a,b}	[20]
AISI 1008 steel/0.85 mm	Multiwalled-carbon-nanotubes (MWCNTs)	Improved by 45% ^a	...	[102]

^a Tensile shear^b Cross tension**Fig. 5** Failure mode after cross tension and tensile shear loading of **a, b** MSS/MSS weld failed in IF and **c, d** MSS/Ni/MSS weld failed in PF mode [92]

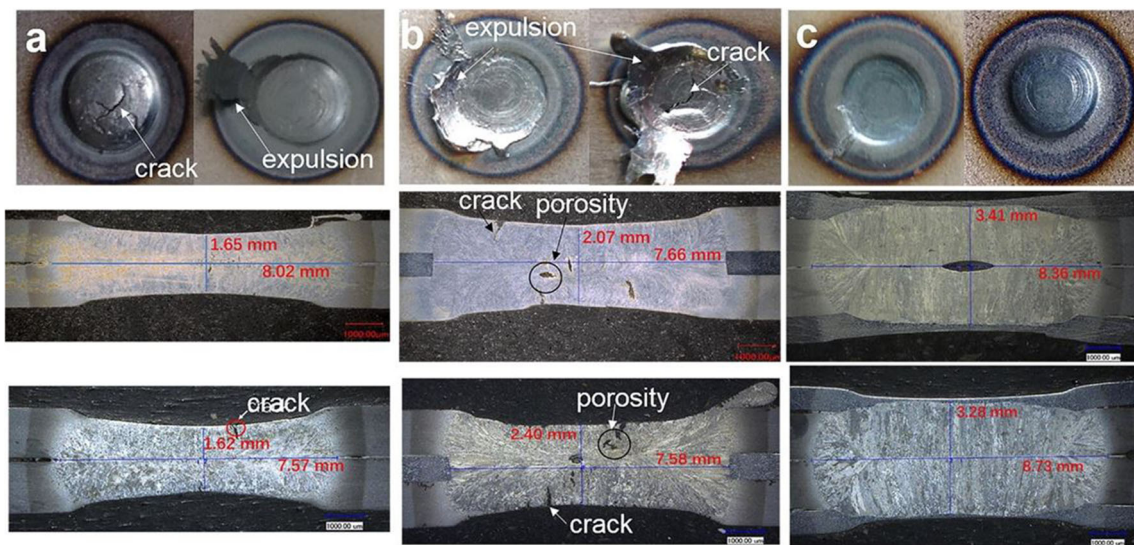


Fig. 6 The nuggets and weld surface obtained in the three welding set-ups. **a** No shim, **b** shim-in, and **c** shim-out [20]

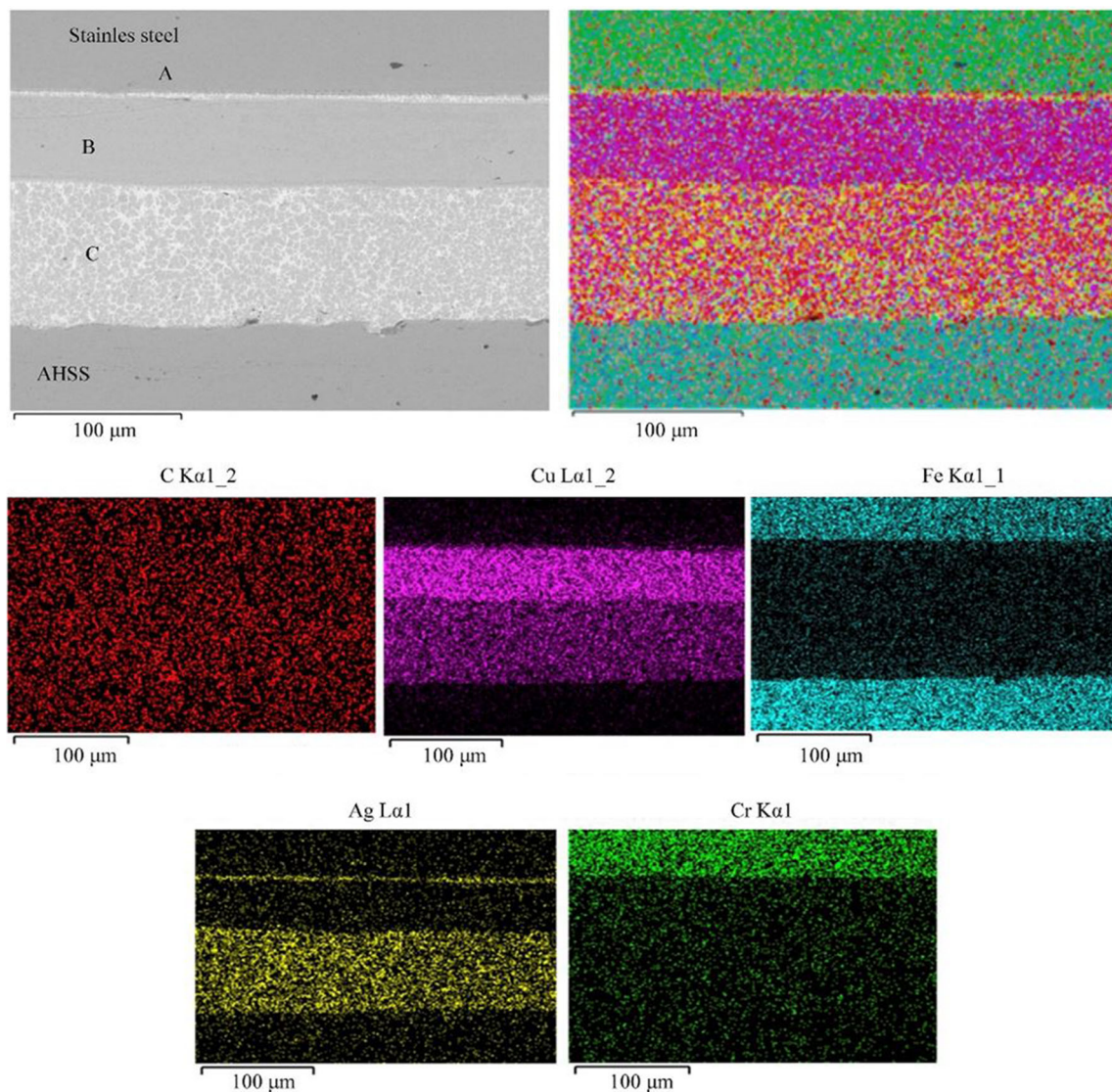


Fig. 7 EDS elemental maps of the joint [100]

2.1 Critical analysis and future research outlook of IA-RSW

Although it is obvious that introducing an interlayer material may reduce the weld brittleness via tuning microstructure/chemistry of FZ and composition of IMCs at weld interface. However, some issues need to be addressed to take full advantage of the process. First, the interlayer material is different from the substrates in melting point and thermal conductivity, so its addition can alter the distribution and transfer of heat to the weldment. Low heat input can result in insufficient fusion of interlayer material and excessive heat input may lead to expulsion. Numerical modelling can help to determine the interface and bulk resistances with regard to temperature change with addition of an interlayer material. Besides, it would also help to calculate the correct amount of heat required to melt the substrate and interlayer material, which in turn helps to optimize the process parameters. Indeed, the addition of interlayer material makes RSW process complex in addition to prolonging the cycle time. Secondly, interlayer insertion would increase the production cost (due to higher energy needed to melt interlayer material plus cost of interlayer material). Third, addition of interlayer material (particularly if mode of insertion is a sheet) adds weight to the vehicle which ultimately then affect fuel economy. Fourth, interlayer insertion can result in un-melted material around the

weldment which can affect the fatigue strength of the joint due to increased number of notches at weld interface. Therefore, further studies are required to understand the fatigue behaviour of IA-RSW joint. Fifth, in real production line, thousands of spot welds are made in very short time; it is required to develop a mechanism for insertion of interlayers between substrate sheets for mass production.

3 Magnetically assisted RSW

In the MA-RSW method, an externally applied magnetic field interacts with the welding current to produce a Lorentz force that strongly drives the molten metal to flow in a specific direction. The schematic of MA-RSW is shown in Figure 8. The stirring affects the flow of molten metal within nugget during melting and solidification in a way so that the oriented growth of the dendrites is less directional, and the faying surface is less visible. The intensive mixing of the liquid metal promotes grain refinement within a weld nugget resulting in improved mechanical performance of the weld compared to the traditional one [104–117].

3.1 Effect of an external magnetic field on the flow behaviour of liquid metal in weld nugget

The working principle of MA-RSW is related to electromagnetic stirring (EMS) of liquid metal inside weld nugget. The Lorentz force, which is the vector sum of induced magnetic force (F_{in}) and external magnetic force (F_{ex}) is the driving force for EMS [104, 111–114, 118] given as

$$F_{MA-RSW} = F_{in} + F_{ex} = J \times B_{in} + J \times B_{ex} \quad (3)$$

where J is the welding current density and B_{in} and B_{ex} are the induced and the external magnetic flux density, respectively. Weld nuggets are formed in traditional RSW by the heat generated due to resistance to electric current flow. The welding current density J induces a magnetic field B_{in} normal to the x - y plane of the weld. The interaction of J and B_{in} produced a magnetic force F_{in} in the x - y plane of the weld, causing the molten metal to flow in four symmetrical loops inside the weld nugget, as shown in Figure 9a [112, 113, 116, 119]. When a pair of permanent magnets is mounted along the electrodes, an external magnetic field B_{ex} is produced that is radially oriented in the x - y plane of the weld and perpendicular to the induced magnetic force F_{in} . The interaction between J and B_{ex} produced a magnetic force F_{ex} which is circumferentially oriented in plane. The resultant magnetic force F_{MA-RSW} drive the molten metal to flow both radially and circumferentially (refer Figure 9b), thus promoting further heat and mass transfer during the welding process [111–113, 116].

The idea of electromagnetic stirring (EMS) of the liquid metal is not new. In past, the external magnetic field has been

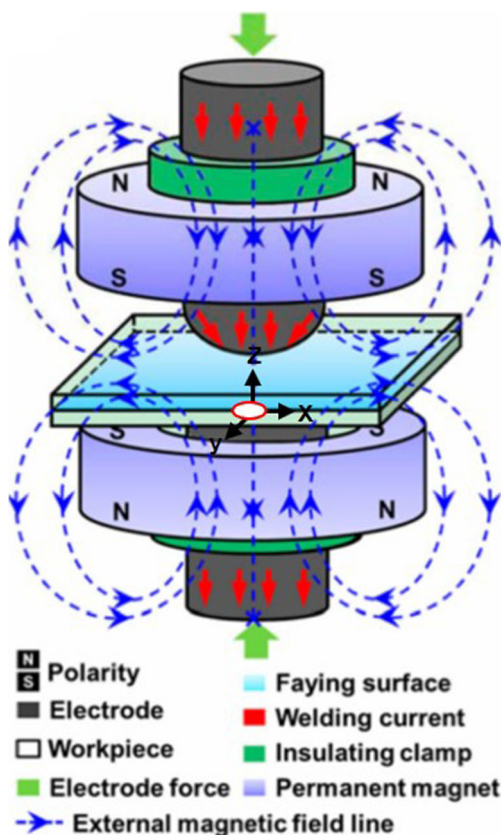
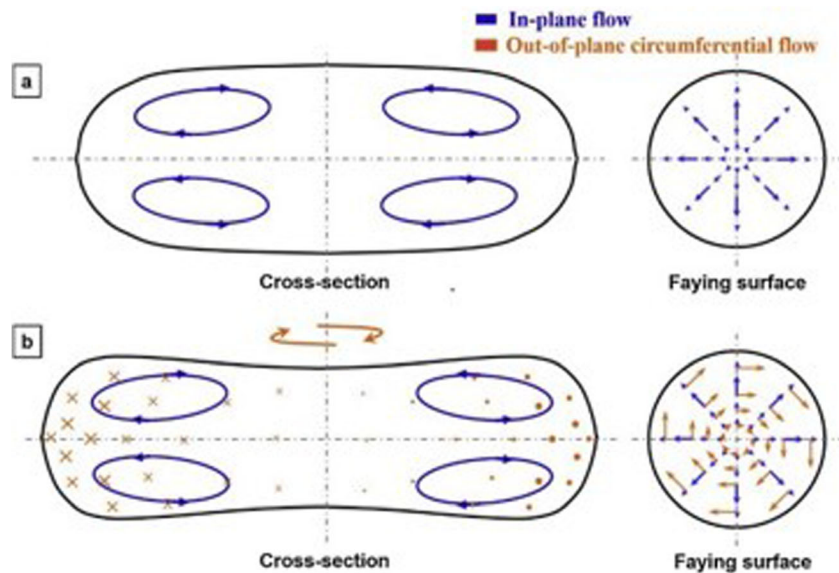


Fig. 8 Sketch of MA-RSW process [104]

Fig. 9 Liquid metal flow pattern in RSW **a** without external magnetic field and **b** with external magnetic field [113]



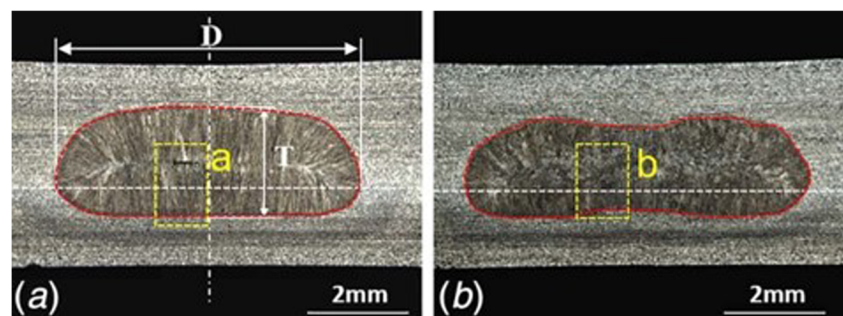
applied to control the melting and solidification of metals in continuous casting, arc welding, and other specific processes [105]. Villafuerte [120] refine the grain structures in gas tungsten arc welds by using the EMS method. Following its effective use in arc welding, EMS has gradually attracted the attention of researchers in the RSW process [115]. Popov [118] first introduce EMS into RSW in 1993. He investigated the effect of a radially oriented magnetic field on 3.5-mm-thick austenitic stainless steel (ASS) resistance spot weld. Results showed that weld made with magnetic field assistance have porosity free nugget resulting in improved impact toughness and fatigue strength compared to weld made using traditional RSW. Watanabe et al. [121] examined the effect of magnetic field direction on the nugget size and microstructure of stainless steel RSWs. Results showed that weld nugget size increased when magnetic field induced in the direction perpendicular to the welding electrodes.

3.2 Mechanism of nugget formation in MA-RSW

Studies [104, 105, 110–116] have shown that nugget in MA-RSW weld is formed in an irregular peanut-shell-shaped

ellipsoid with two ends slightly thicker than the middle. Moreover, the nugget is slightly increased in its long axis (i.e. diameter) compared to regular ellipsoid-shaped nugget in traditional RSW, as illustrated in Figure 10. The variation in shape and size of the nugget is due to the difference in flow of liquid metal during the nugget growth and solidification process. During the traditional RSW process, the liquid metal only makes rotational motion in four symmetric cells driven by the induced magnetic force (F_{in}) circumferentially oriented in the x - y planes of the weld. However, when an external magnetic field is applied, a magnetic force F_{ex} is produced and acts normal to the axisymmetric plane of the weld. The resultant magnetic force F_{MA-RSW} then drives the liquid metal not only in the rotational flow but also flow centrifugally inside the nugget. The mixed flow brings more liquid metal from the nugget centre to nugget edge. Eventually, it results in the peanut-shell-shaped nugget characteristically wider at edges and thinner at the centre [111, 112, 115, 116]. However, it has been reported that the high-speed movement could fly away the liquid metal from the nugget due to increase in pressure gradient inside the nugget leading to expulsion. The risk of expulsion increases at higher welding current and time [111, 113]

Fig. 10 Macrostructure of welds: **a** traditional RSW; **b** MA-RSW [114]



3.3 Effect of external magnetic field on microstructure, microhardness, and mechanical performance of RSW joint

It is well reported in literature that EMS decreased the directionality of columnar grains and a refined grain structure is formed in FZ of MA-RSW weld [104, 105, 111–113, 115, 116]. Also, the faying line in MA-RSW weld disappears due to change of the solidification mode, i.e. from sequential solidification mode to simultaneous solidification mode [114]. All microstructural changes in MA-RSW can be explained based on the flow patterns of the molten metal. During the heating stage, the temperature difference inside the nugget is greatly decreased by the circumferential flow of molten metal which results in homogeneous nucleation, and thus, the number of equiaxed grains increases. During the initial cooling stage, the inertial movement of the solidifying metal breaks the growing dendrites, which results in the relatively disordered crystal orientation [104, 114]. Figure 11 shows the microstructure of FZ of a DP780 steel MA-RSW weld exhibiting the formation of refined grain structure compared to columnar grain structure of traditional RSW.

Apart from grain refinement, applying external magnetic field also results in elimination of shrinkage void/cavity in nugget centre and causes uniform microhardness distribution of FZ [111–114]. Li et al. [111] reported that in traditional RSW, the electrode force cannot deform the solidified metal due to the high stiffness of the columnar grains; therefore, shrinkage cavities are formed in typical RSW weld nuggets at the end of solidification. However, for the MA-RSW weld, the less directional solidified grains in the nugget greatly enhance the plasticity of the solidified metal; thus, the shrinkage

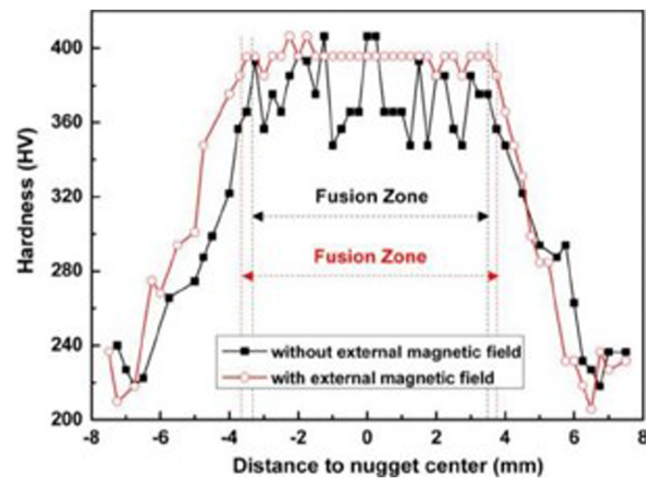


Fig. 12 Microhardness distribution in DP590 steel weld [116]

cavities in the nugget are merged under the assistance of the electrode force. The uniform microhardness distribution of MA-RSW has been attributed to equiaxed grain structure and possible reduction of elemental segregation resulting from strong stirring of liquid metal in weld nugget, as shown in Figure 12. The improved mixing of alloying elements and the reduced cooling rate fosters the elemental distribution [115, 116]. In opposite to this finding, Li et al. [112] reported that external magnetic field causes elemental segregation of Cr and Ni in austenitic stainless-steel weld even cooling rate becomes slowed down and reduced temperature gradient occurs.

The refinement of grain structure, elimination of shrinkage cavity, and reduction of elemental segregation in FZ results in better mechanical performance of MA-RSW compared with traditional one. Table 2 compares the peak load and failure mode of welds subjected traditional RSW and MA-RSW of

Fig. 11 Microstructure of FZ of DP780 steel weld: a, b traditional RSW and c, d MA-RSW [115]

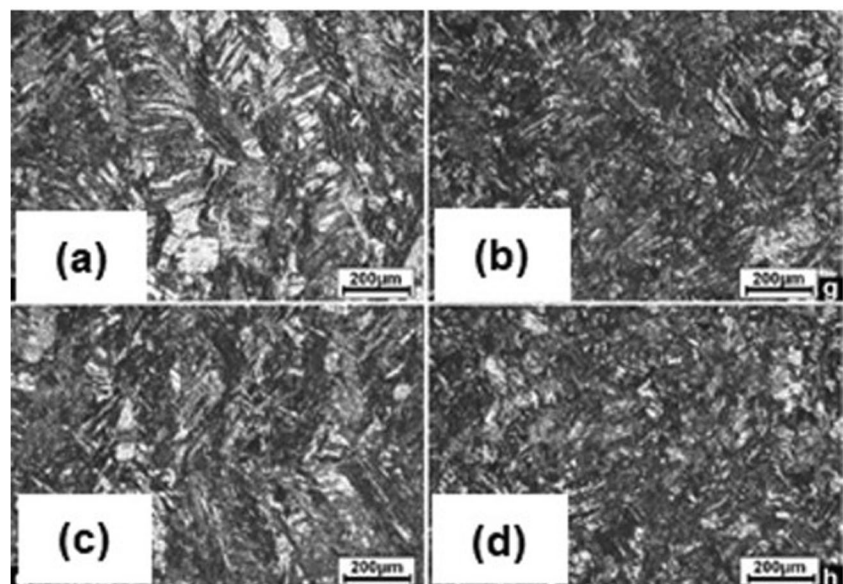


Table 2 Comparison of peak load and failure mode between RSW weld and MA-RSW weld of different grades of steel

RSW			MA-RSW			
Work piece material/thickness	Peak load (kN)	Failure mode	Magnet material/shape	Peak load (kN)/percent improved compared to RSW	Failure mode	Ref
ASS/2.5 mm and EN4318/1.5 mm	IF ^a	N52/Arc	8.9% ^a	PF ^a	[114]
DP780 steel/1.8 mm	IF ^a	N35/Ring	3.68% ^a	IF ^a	[111]
DP590 steel/ 2.25 mm	30.4 ^a	N40/Ring	32.6 ^a	[116]
ASS-HT/5 mm and ASS-DLT/4 mm	83.3 ^a	IF ^a	N40/Ring	90.7 ^a	IF ^a	[112]
DP590 steel/1.6 mm	IF ^a	N52/Circular bilateral	24.7% ^a	IF ^a	[113]
DP980 steel/0.8 mm	IF ^a	N40/Ring	6.95% ^a	IF ^a	[105]
DP780 steel/1.25 mm	15.8 ^a 7.3 ^b	PF ^{a,b}	NdFeB/Ring	17.7 ^a 9.3 ^b	PF ^{a,b}	[115]

N35, N40, and N52 are different grades of neodymium iron boron (NdFeB) magnets

^a Tensile shear

^b Cross tension

different automotive steels. Besides, studies [113, 115] have shown that MA-RSW weld exhibits longer fatigue life than traditional RSW. Figure 13 shows fatigue test results of DP590 steel welds subjected to traditional and MA-RSW. It can be observed MA-RSW shows higher fatigue life than the traditional one.

3.4 Critical analysis and future research outlook of MA-RSW

The use of the externally applied magnetic field is still a new subject in RSW field and mostly been focused on similar steel welding. However, the research relating to dissimilar alloy welding is lacking. Today's vehicle body structure is made of different alloy combination such as different AHSS grades,

AHSS to Al alloys and AHSS to Mg alloys. In case of dissimilar weld, metals have different electrical and thermal conductivity, density, and solubility at specific temperature, which can affect the flow behaviour under the applied magnetic field. Another concern for MA-RSW is that long welding time is required to strengthen the stirring effect of the external magnetic field which ultimately increases the process time. In addition, longer welding time can increase the wear of electrode tip due to longer contact time with hot metal. Therefore, welding time should be minimized at possible extent. To proper control the external magnetic field intensity during welding, magnetic apparatus such as electromagnet needs to be design so that optimum conditions can be set for a particular alloy weld. It is well known that the direction of the magnetic field depends upon the direction of current flow; i.e. a DC source generates a magnetic field of constant polarity and an AC source generates alternating magnetic field whose polarity changes. The liquid metal flow in weld nugget can be tuned via changing magnetic field by changing current polarity in an electromagnet. For that purpose, further research studies are needed to understand the flow behaviour under constant and changing magnetic field.

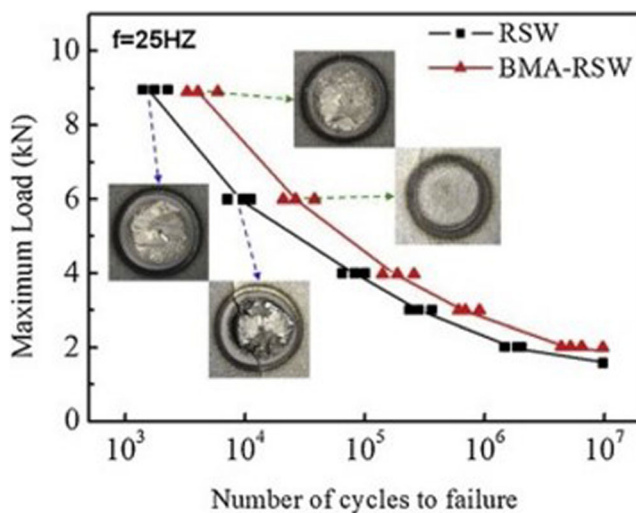


Fig. 13 Fatigue test results of traditional RSW and MA-RSW welds [113]

4 Pulsed-RSW

Pulsed-RSW is considered as a potential approach to produce a tough microstructure in the FZ and to alleviate the problem of high sensitivity to IF mode of the AHSS RSWs [122–125]. This approach in RSW is termed in different ways, e.g. in situ postweld heat treatment (PWHT) [52, 63, 126–128], double/multi pulse RSW [49, 69, 122–125, 129–136], second pulse RSW [137, 138], electrothermal treatment [139],

and in situ or in-process tempering [51, 83, 140, 141]. In this method, during welding, a second pulse (in some cases more than two pulses) is applied just after the primary (or first) welding pulse to alter the microstructure of weld nugget. The first pulse current and time are selected to make the target nugget size, and then after quite short cooling (current-off), the post-heating/second pulse current is applied for a specific time. This method is considered a relatively simple way of reducing the weld brittleness and to improve the mechanical performance of the weld joint. Depending upon temperature and base metal chemistry, pulsed-RSW results in following phenomena.

- (i) Martensite tempering. Tempering of martensitic structure of FZ/HAZ. This phenomenon occurs when the peak temperature during in situ PWHT is below A_{c1} temperature [52].
- (ii) Martensite refining at weld nugget edge. Transformation of cast-like microstructure (i.e. consisting of large columnar/dendritic grains) to semi equiaxed structure at outer periphery of weld nugget. This mechanism is activated when the peak temperature between A_{c3} and melting temperature [49, 52, 122].
- (iii) Reduction of elemental segregation. Uniform distribution of P, S, Si, and Mn at weld nugget edge. This is diffusion-based phenomenon and occurs when the peak temperature is above A_{c3} and below melting temperature [49, 68, 69, 122].
- (iv) Ferrite-austenite phase balance in DSS weld. A balanced microstructure with high austenite proportion and minimal Cr_2N intermetallic precipitates can be obtained in the FZ of DSS by adopting pulsed RSW [63].
- (v) Reduction of liquid metal embrittlement severity. Controlling the input of the welding cycle via using the pulsed-RSW schedules can reduce LME severity while still maintaining the required minimum nugget diameter [142, 143].

Although mechanical properties of the spot welds can be improved via different metallurgical mechanisms, yet the selection of an improper second pulse current and time can have adverse effects on the mechanical properties of the weld due to re-austenitization/remelting of the entire weld nugget leading to un-tempered martensite [33, 52, 126].

4.1 Effect of in situ PWHT on martensite tempering and mechanical properties of the weld

Tempering of martensite reduces the hardness and improves the ductility of weld nugget. Therefore, tempering temperature is of immense significance. The tempering temperature must not be too high so that austenite is formed. However, the

temperature must be high enough to let reinforced solute atoms of carbon in the martensite to precipitate out of the phase to create carbides. In RSW, the weld nugget can be tempered if the second pulse is generating the right amount of heat into the weld. The optimal current level and current time of a temper pulse vary with alloy composition [50]. Generally, two types of in situ tempering schemes are used, i.e. (i) tempering at low current and long pulse time (also known as conventional tempering) and (ii) tempering at high current and short pulse time (also known as spike tempering) [144, 145]. Conventional tempering is considered less feasible for production in automotive industries as it requires long heating times which decreases the RSW process efficiency [49, 145]. On the other hand, for spike tempering, it is necessary to carry out cooling process over a long time and thus issues of operational efficiency remain unresolved [144]. The advantage of rapid heat treatment using the pulsed-RSW process is lost if the time required to obtain the desired microstructure is too large. Many researchers have recommended a criterion for reducing process time and performing adequate quench and tempering treatment on the weldment, according to which the cooling time (time between the first melting pulse and the second tempering pulse) should be chosen so that the weldment is cooled slightly below the martensite finish temperature (M_f) before being heated again [51, 126, 140, 146]. The tempering current and time are then adjusted so that martensite tempering occurs to a sufficient extent to reduce FZ hardness. Inadequate cooling time prevents the complete martensite transformation, allowing it to form martensite on final cooling at the end of the temper cycle. Table 3 compares the peak load, energy absorption and failure mode of the welds subjected to traditional single RSW and pulsed-RSW methods.

Measurement of the temperature and current distribution, heating, and cooling rates is very difficult for RSW because of short welding time and invisible liquid nugget and becomes much complicated when post heating cycle is applied. However, numerical models based on finite element methods can be used as guide to determine tempering temperature, heat distribution, and cooling rate during main and postweld heating pulse. Taniguchi et al. [144] measured temperature and current distribution at long cooling time (200 cycles) during conventional and spike tempering using finite element analytical software SORPAS. In each case of tempering, the post-heating conditions were set so that the value for heat input Q is same. The heat inputs were estimated from the post heating cycle current and time using following expression:

$$Q = \left(\frac{I_t}{I_m} \right)^2 \left(\frac{T_t}{T_m} \right) \quad (4)$$

where Q is heat input, I_m is main current [6.5 kA], I_t is tempering current [kA], T_m main heating time [18 cycles], and T_t

Table.3 Comparison of peak load, energy absorption and failure mode between RSW weld and Pulse-RSW weld of different grades of steel

Work piece material/ thickness	RSW				Pulsed-RSW				Ref
	Main pulse WC and WT	Peak load (kN)	Energy absorption (J)	Failure mode	Postweld pulse WC and WT	Peak load(kN)/ percent improved compared to RSW	Energy absorption (J)/ percent improved compared to RSW	Failure mode	
AISI420 MSS/1.5 mm	8 kA 0.24 s	6.7 ^a 1.3 ^b	2.6 ^a 0.6 ^b	IF ^{a,b}	4 kA 1.4 s	77% ^a 102% ^b	240% ^a 1030% ^b	PIF ^a IF ^b	[141]
AISI420 MSS/1.5 mm	8 kA 0.24 s	6.5 ^a 1.3 ^b	2.6 ^a 0.6 ^b	IF ^{a,b}	5 kA 0.24 s	83% ^a 127% ^b	318% ^a 1460% ^b	PIF ^a IF ^b	[126]
DP590 steel/1.8 mm	7.5 kA 560 ms	10.63 ^b	161.19	PF ^b	7.5 kA 560 ms	62% ^b	62.3% ^b	PF ^b	[51]
DP600/1.4 mm	8.5 kA 400 ms	8.13 ^b	PF ^b	5.1 kA 1300 ms	11.94 ^b	PF ^b	[125]
DP590 steel/1.5 mm	9.3 kA 280 ms	16.72 ^a	PF ^a	17.76 ^b	PF ^b	[135]
980 MPa AHSS/1.3 mm	6.6 kA 320 ms	3.8 ^b	PIF ^b	6.6 kA 320 ms	5.7 ^b	PF ^b	[148]
Q&P980 steel/1.8 mm	7 kA 240 ms	4.9 ^b	28.43	PIF ^b	6 kA 240 ms	6.44 ^b	54.49	PIF ^b	[123]
TRIP800 steel/1 mm	8 kA 20 cycle	15.3 ^a	IF ^a	7 kA 20 cycle	16.4 ^a	PF ^a	[137]
DP1000 steel/1.5 mm	8 kA 380 ms	9.2 ^b	55.3 ^b	PF ^b	8 kA 380 ms	11.7 ^b	75.2	PF ^b	[49]
Hot stamped steel/1.2 mm	5 kA 250 ms	IF ^a	6 kA 250 ms	Improved	Improved	IF ^b	[129]
1 GPa complex phase steel/1.3 mm	6.2 kA 320 ms	PIF ^a IF ^b	6.2 kA 320 ms	Improved ^{a,b}	PF ^{a,b}	[122]
HSLA350 steel/1.4 mm	8 kA 280 ms	7.8 ^a	28.9	PF ^a	4 kA 280 ms	8.9 ^a	43 ^a	PF ^a	[127]
SAPH440 steel/2 mm	12 kA 13 cycle	IF ^a	8.5 kA 30 cycles	Improved ^a	PF ^a	[33]
DP980 steel/1.6 mm	5.5 kA 280 ms	7 ^b	PIF ^b	8.3 kA 60 ms	11 ^b	PF ^b	[145]
Hot stamped steel/1.4 mm	6 kA 375 ms	15.3 ^a 6.5 ^b	PIF ^{a,b}	5 kA 375 ms	17.8 ^a 8.5 ^b	PF ^{a,b}	[130]
7 Mn AHSS /1.4 mm	1.5	IF ^b	3.7 ^b	IF ^b	[149]

WC welding current, WT welding time, and PIF partial interfacial failure

^a Tensile shear

^b Cross tension

tempering heating time [cycles]. Figure 14 shows the temperature and current density distribution of conventional tempering ($I_t = 6$ kA and $T_t = 0, 10$, and 20 cycles). They reported that when the weld was cooled to 50 °C or lower after the nugget had been formed, heat distributed from nugget centre towards outer periphery and increases with increase of T_t . As a result, temperature at nugget centre is higher than outer periphery. Conversely, the current density was a little higher near the outer periphery of the nugget than at the centre of nugget and there was little change in current density with increase in T_t .

Figure 15 shows the temperature and current density distribution of spike tempering ($I_t = 26.9$ kA and $T_t = 0$ and 1 cycle). Again, they found that nugget is heated at a higher temperature compared to conventional tempering even when the post-heating time is only one cycle. Unlike conventional

tempering, both temperature and current density are higher at the vicinity of the electrode-nugget periphery and between the sheets than the centre of nugget. Since the final temperature distribution is affected by heat conduction, therefore, the cooling is greater at the electrode and point of contact between sheets. As a result, the temperature rise was inhibited at these points so that temperature of the sheet interior was rather higher than its surface.

Based on spike tempering process, JFE steel developed “Pulse Spot™ welding,” by utilizing the heat generation phenomenon in the area around the nugget in short-time high-current post-heating [147]. This technology makes it possible to obtain improved weld joint strength in a shorter time than with conventional temper pattern. It is reported Pulse Spot™ welding process significantly reduces tempering time. Therefore, it is considered to be a much

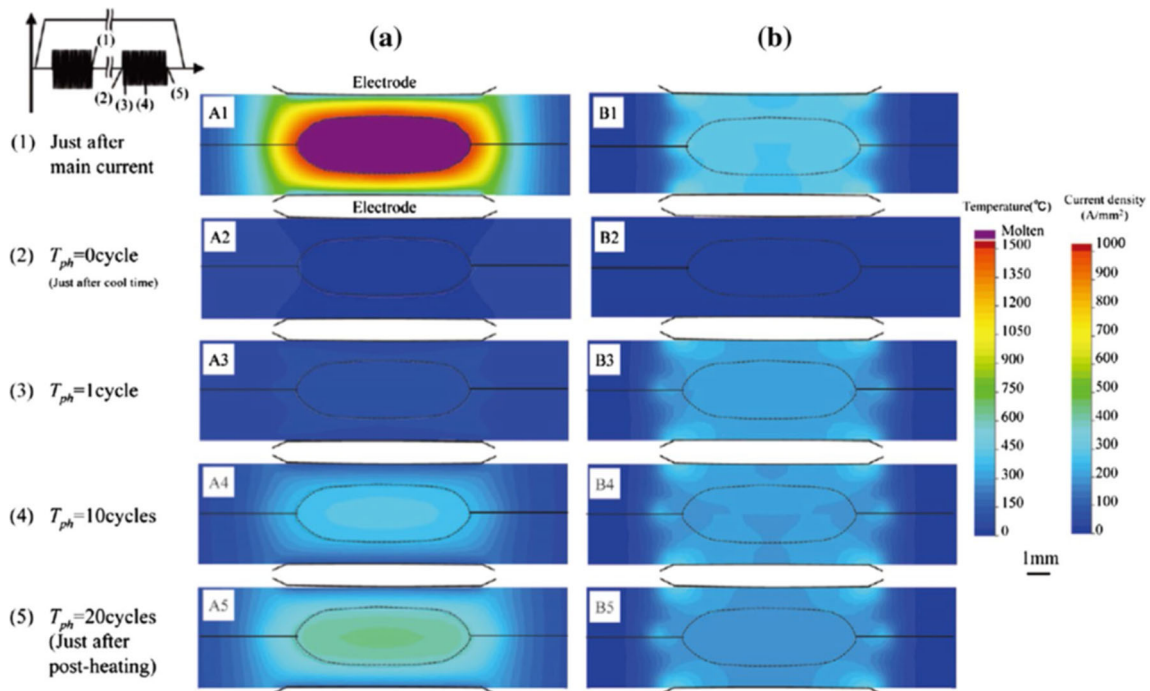


Fig. 14 Simulated temperature and current density distributions in ultra-high strength steel sheet for conventional tempering [144]

more viable option to be introduced in the car assembly line.

In the past, several authors have recommended different pulsed-RSW schemes to temper the martensitic microstructure with aim to increase the toughness of AHSS RSWs. An

earlier work in this regard was carried out by Chuko and Gould [146]. They developed temper diagrams based on welding current vs welding time of two DP steels, as shown in Figure 16. Hardness was related for evaluating the effectiveness of tempering. According to the diagrams, the optimal

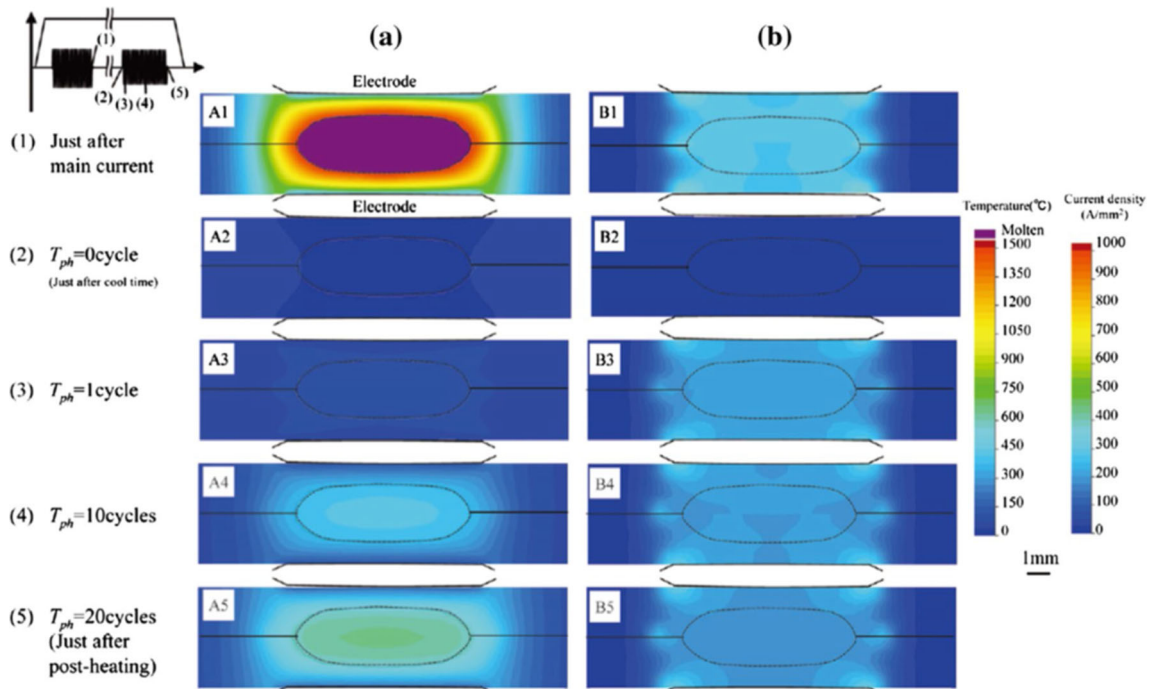


Fig. 15 Simulated temperature and current density distributions in ultra-high strength steel sheet for spike tempering [144].

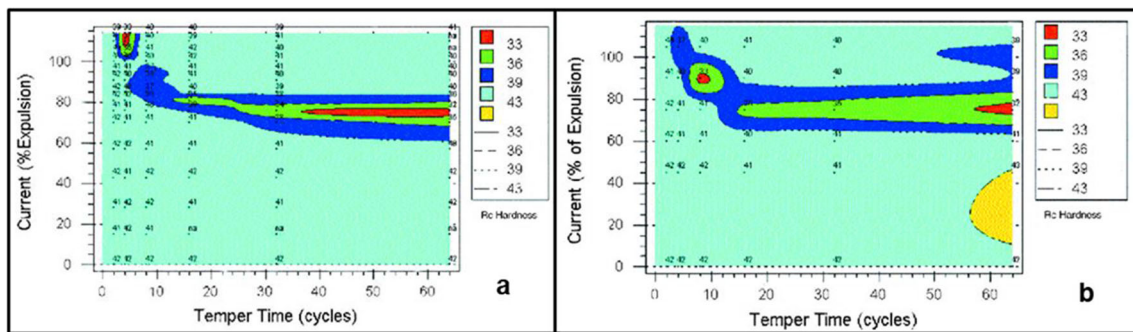


Fig. 16 Temper diagram for RSWs of **a** DP690 steel and **b** DP960 steel [146]

temper current is 75–80% of the expulsion current and the optimal temper time is 600–700 ms. These temper diagrams can be used as reference guide to substantially reduce weld hardness and hold time sensitivity of AHSS RSWs.

Recently, Aghajani et al. [126] reported that applying a second pulse current of 5 kA resulted in martensite tempering in FZ of AISI420 martensitic stainless steel resistance spot weld. Due to tempering of martensite, the microhardness of FZ dropped by ~15% compared to conventional single pulse weld (SPW). It was found that tempering of martensite enables the formation of nano-sized carbide which are essentially $M_{23}C_6$ (where M refers to Cr or Fe) at both weld nugget centre and nugget edge, as shown in Figure 17. Reduction in hardness resulted in improved fracture toughness of FZ and causes enhancement in peak load and energy absorption under TS and CT loading. A dimple like fracture was observed in double pulse weld (DPW) compared to cleavage fracture in SPW. A similar finding has been reported in Ref [141].

Wakabayashi et al. [83] found that grain size in the HAZ increased with application of a prolonged second pulse current, thus promoting the auto-tempering of martensite in HAZ of a high strength steel resistance spot weld. They found that tempered martensite structure prevents the propagation of crack into the nugget, thus leading to improved peak load and PF mode. Soomro et al. [51] examined the effect of in situ PWHT parameters, i.e. second pulse current, second pulse time and cooling time on microstructure, microhardness, and CT performance of DP590 steel resistance spot welds. Results showed that an improvement of 62% in peak load and 62.3% in energy absorption was achieved at optimum conditions. The weld failed in PF mode at optimum postweld heating condition compared to IF mode of traditional single pulse weld. Improvement in mechanical properties was attributed to (i) enhanced nugget size which in turn results in higher load bearing area and (ii) tempering of martensite in FZ and HAZ leading to improved toughness of the weldment. Wang et al. [135] reported that low carbon α -phase and transition carbides (mainly ϵ -carbide) were formed after applying in situ PWHT on DP590 steel resistance spot weld, leading to improved tensile shear peak load. However, the weld failed in IF mode. Wei et al. [150] found that tensile shear peak load and energy

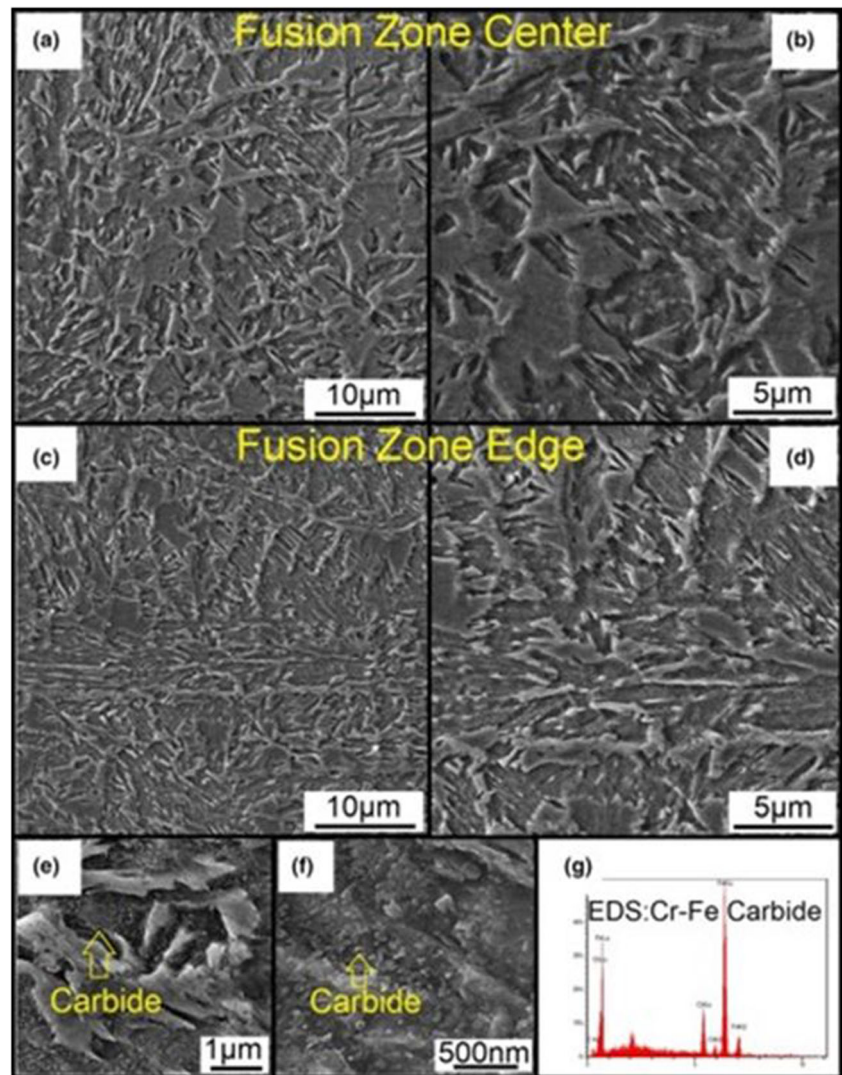
absorption of DP/TRIP dissimilar steel RSW joint increased due to tempering of martensite in weld nugget when subjected to in situ PWHT.

4.2 Effect of in situ PWHT on martensite refining in FZ and mechanical properties of RSW joint

One of the most widely reported phenomena that occurs during in situ PWHT of AHSS resistance spot welds is formation of a thin shell (also known as annealed zone/REX zone) at periphery of the weld nugget [49, 122, 127, 131–133, 137, 140]. A schematic representation of a cross-section of the weld subjected to pulsed-RSW is shown in Figure 18. During the first pulse, the primary weld nugget is produced with large columnar grain structure. Applying second pulse current results in a re-melted zone inside the primary weld nugget, forming a secondary weld nugget. The REX zone differs in grain size depending upon the second pulse current and time applied [122]. The formation of two distinct zones in weld nugget is caused by a non-uniform temperature distribution during in situ PWHT. It has been reported that the temperature distribution in the spot weld during in situ PWHT is roughly parabolic in shape, with the peak temperatures always on the weld centerline [140]. Therefore, the centre of the weld nugget is re-melted during heating as the temperature reaches melting point and then retransformed into solidification columnar grains consisting of hard lath martensite upon cooling. The outer periphery of weld nugget is re-austenitized and retransformed into semi equiaxed grains martensite grains as the temperature remains between Ac_3 and below melting point [52, 122].

Eftekarimilani et al. [122] found that applying second pulse current results in partial remelting of the FZ centre and re-austenitized the edge of FZ during pulsed-RSW of 1 GPa complex phase steel. Secondary FZ exhibits a solidification structure consisting of dendrites, and the annealed zone reveals an equiaxed grain structure consisting of martensite, as shown in Figure 19. The microstructural change resulted in improved peak load under TS and CT loading and promoted PF mode. Moreover, annealed zone in DPWs exhibits slightly lower microhardness compared to secondary weld nugget.

Fig. 17 17 Electron micrographs of DPW **a, b** center of FZ and **c, d** edge of FZ, **e, f** carbide precipitation in the nugget edge, and **g** EDS profile of carbide particles [126]



Soomro and Pedapati [127] also found that applying second pulse current subdivided the weld nugget of HSLA350 steel into two zones, i.e. columnar grain zone (CGZ) composed of lath martensite in the inner core and quasi equiaxed grain zone (EGZ) composed of ferrite and martensite in the outer layer. Results showed that an increment of 14.1% and 48.79 % was achieved in tensile shear peak load and energy

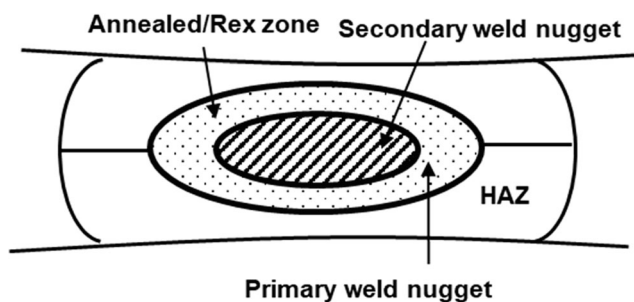


Fig. 18 Schematic of weld cross section subjected to high temperature in situ PWHT

absorption, respectively, compared to SPW. Moreover, a reduction of $\sim 13.2\%$ in microhardness of EGZ was observed compared with CGZ of DPW. Chabok et al. [49] reported that after applying a second pulse current, the initial FZ of DP1000 steel RSW was subdivided into two zones. The inner zone showed columnar grains, while the outer REX zone composed of equiaxed grains consisting of lath martensite, as shown in Figure 20. They found that double pulse weld showed an improvement of $\sim 27\%$ and $\sim 49\%$ in CT peak load and energy absorption, respectively, compared to single pulse weld. Furthermore, the microhardness of the Rex-zone was reduced by 6.6% compared to inner zone of the double pulse weld. Although both welds failed in PF mode, yet single pulse weld failure occurs at the CGHAZ adjacent to the FZ and DPW failure occurs from two side of weld.

In another study, Baltazar et al. [137] found that applying second pulse current of 7 kA resulted in 7% improvement of TS peak load compared to SPW of TRIP steel resistance spot weld. The improvement in peak load was attributed to

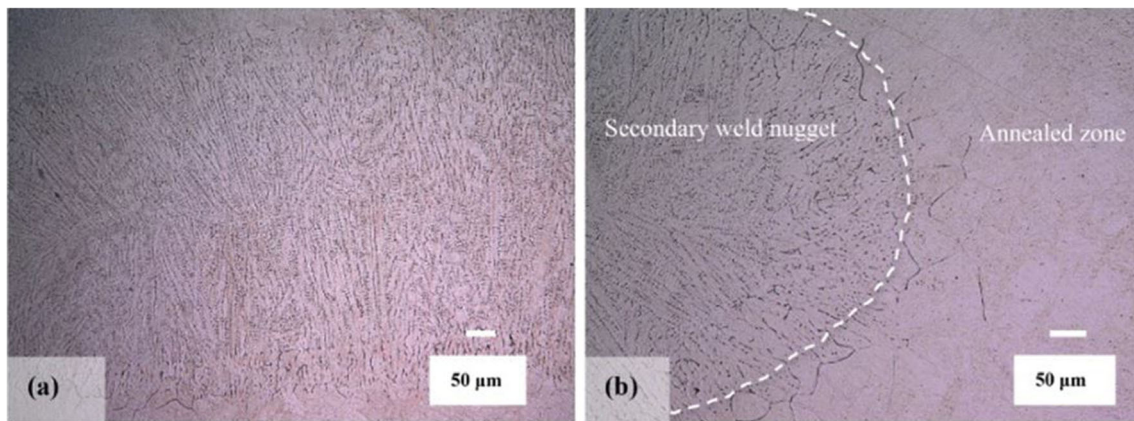


Fig. 19 Microstructure of weld nugget of DPW: **a** secondary weld nugget; **b** annealed zone [122]

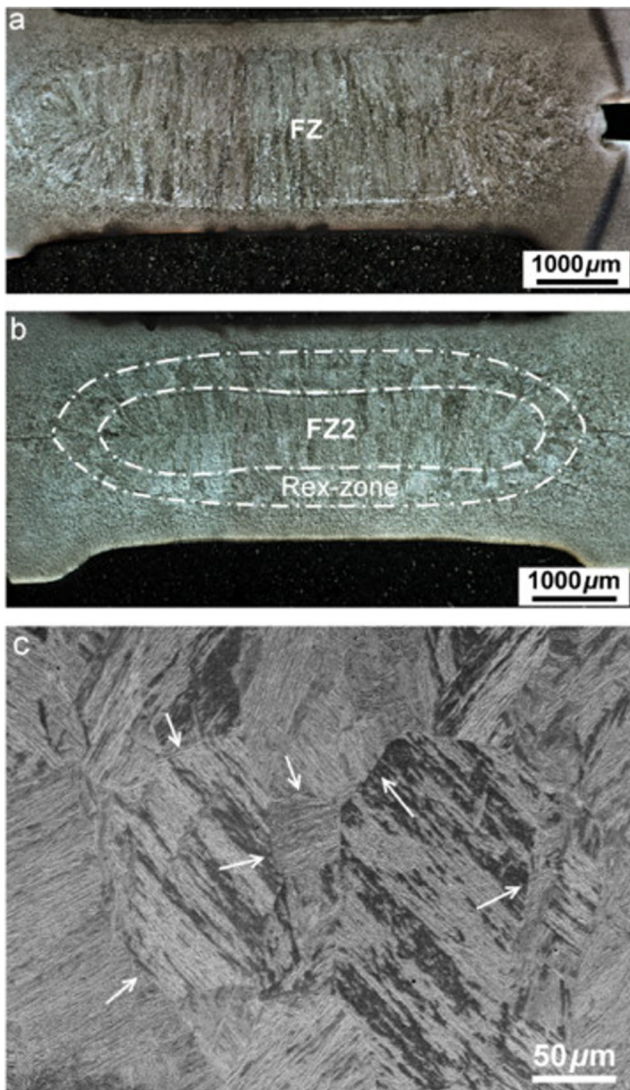


Fig. 20 Optical image showing the cross-section of **a** SPW, **b** DPW, and **c** SEM image showing microstructure of the Rex-zone of DPW with arrows indicating the PAG boundaries [49]

formation quasi equiaxed grains at periphery of the weld nugget which promotes PF mode. Sawanishi et al. [145] applied two postweld pulses with current value of 8.3 kA on DP980 steel RSW joint. They found that CT peak load was improved by 57 % compared to SPW. The improvement in peak load was attributed to the formation of refinement of grain structure at nugget edge which causes restriction to crack propagation promoting the complete PF mode, as shown in Figure 21. However, no hardness reduction was observed in FZ of DPW.

Although it is well-recognized phenomenon that applying a second pulse current on RSW joint produced an annealed zone outside the weld nugget periphery, some studies have shown that applying second pulse current produced an annealed zone in centre of weld nugget, while outer edge remains unaffected. Liu et al. [123] investigated the effect of second pulse current on microstructure and mechanical properties of Q&P 980 steel resistance spot weld. Results showed that weld treated with second pulse current of 6, 6.5, 7, and 7.5 kA exhibited two distinct nugget, primary nugget at the edge and secondary weld nugget in the centre of the FZ, as shown in Figure 22. Secondary nugget exhibits equiaxed grains of martensite and primary nugget showed columnar grains of martensite, as shown in Figure 23. The formation of secondary nugget was attributed to recrystallization of austenite during in situ PWHT. DPWs showed improved TS and CT load-bearing and energy absorption capacity compared to SPW. However, no significant change in microhardness of FZ in DPWs was observed compared to SPW. Furthermore, they found that applying second pulse current of 7.5 kA transforms the failure mode from IF mode to partial thickness-partial pullout (PTPP) mode under TS loading.

In another study, Sajjadi-Nikoo et al [52] found that applying a second pulse current of 5.5 kA transformed the columnar grains to equiaxed grains of martensite in the centre of FZ of TRIP700 steel resistance spot weld. The weld showed improved CT peak load and energy absorption and failed in PF compared to SPW that failed in IF mode.

Fig. 21 21 Cross sections of welds after TS test: **a** SPW failed in partial interfacial (PIF) failure mode; **b** DPW failed in PF mode [145]

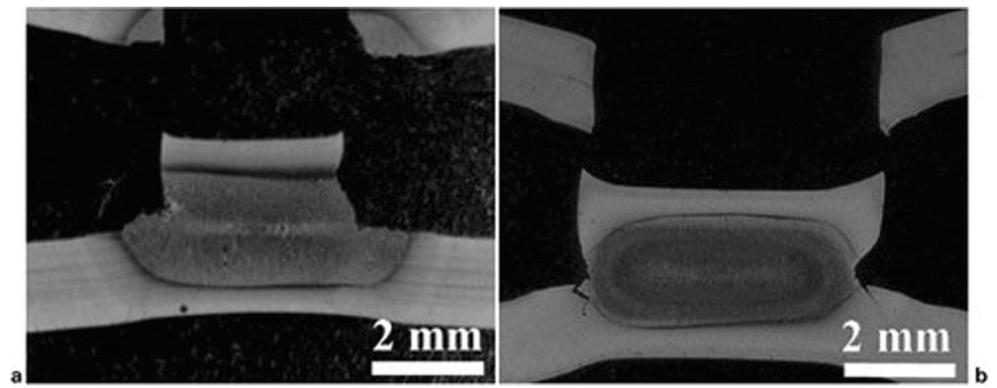
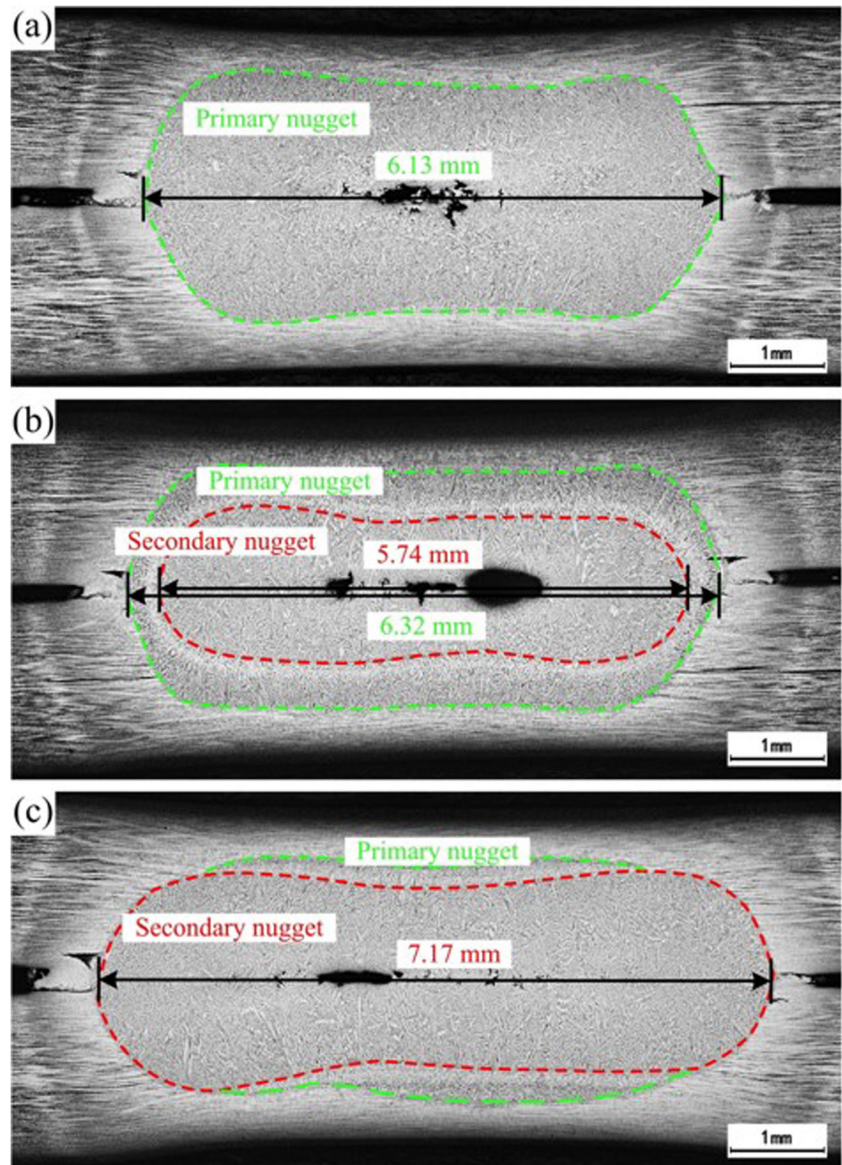


Fig. 22 Weld cross sections: **a** SPW; **b** DPW-6kA; **c** DPW-7.5kA [123]



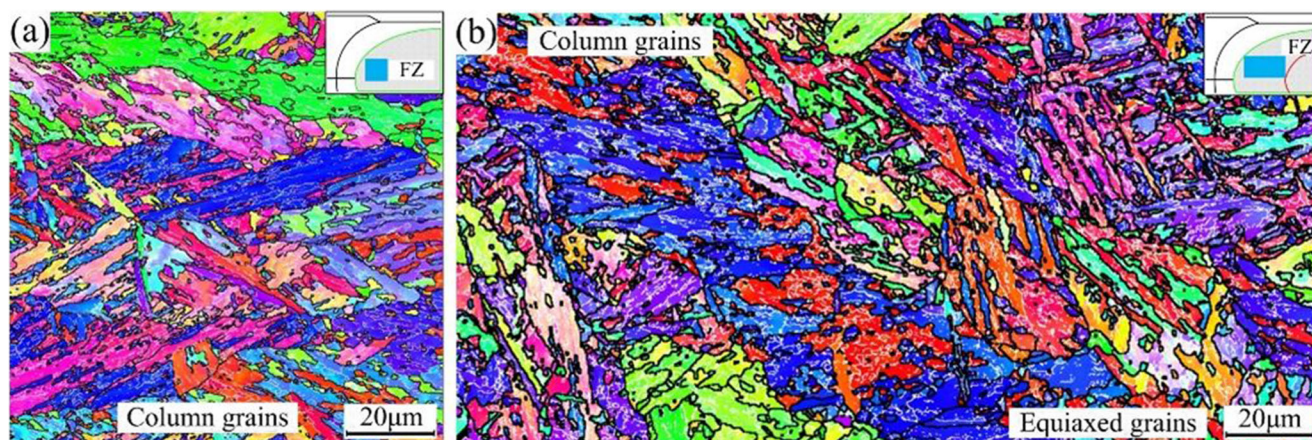


Fig. 23 EBSD image of a SPW and b DPW-6 kA [123]

4.3 Effect of in situ PWHT on crystallographic features of martensite and failure behaviour of RSW joint

It is well known that large columnar grains formed in FZ of AHSS resistance spot weld decrease the fracture toughness of the weld and provide a preferred path for interfacial fracture (i.e. easy crack propagation along the sheet/sheet interface) [66]. The destruction of columnar grains and formation of complete/semi equiaxed grains at weld nugget periphery can impede the crack propagation through weld nugget resulting in PF mode with improved mechanical properties [52]. The fracture toughness of the pulsed-RSW joint is strongly affected by the parameters which determine the mechanical properties of martensite formed at weld nugget edge. The speed of a propagating crack is influenced by toughness of martensitic structure. When martensite is tough, the microstructure is resistant against crack propagation and the mean crack velocity is reduced [49]. Therefore, failure mechanism of AHSS resistance spot weld is strongly dependent on the morphological and crystallographic features of martensite formed in coarse grain heat affected zone (CGHAZ) of SPW and CGHAZ and REX zone of DPW [49, 122].

Lath martensite is the most commonly found microstructural constituent in FZ of many AHSS resistance spot weld. Figure 24 depicts the subgrain structure of lath martensite consisting of packets, blocks, sub-blocks, and laths. The basic crystallographic unit of lath martensite is the lath. Within a single prior austenite grain (PAG), different crystallographic lath variants may exist. Blocks are made up of parallel laths with two different versions, and packets are made up of parallel blocks of the same habit plane [151, 152]. The Kurdjumov-Sachs (K-S) orientation relation predicts that a single PAG can produce 24 distinct crystallographic variants of lath martensite, which can be classified into three Bain groups based on compression axes. [49, 151]. PAG size and the variant have a significant effect on the mechanical properties of lath martensite structures and thus on failure

behaviour of automotive steel resistance spot weld. It has been shown that the finer the PAGs, smaller will be the packet size of martensite, and consequently, the higher the strength and the hardness values of the martensite [152]. These martensitic features along with dislocation density are influenced during in situ PWHT. During the martensite-austenite reversion process upon rapid heating, the austenite nuclei density is substantially increased leading to refining the PAGs, subsequently transforming to finer martensite packets upon cooling [52].

Chabok et al. [49] investigated the effect of second pulse current (i.e. 8 kA) on DP1000 steel resistance spot weld and found that crack in the SPW immediately deflected towards the CGHAZ while crack penetrates small distance into the Rex-zone and then deviate towards CGHAZ in DPW, as shown in Figure 25. Moreover, DPW showed higher CT peak load and energy absorption capacity compared to SPW. Three factors were attributed for enhanced mechanical properties of DPW: (i) During double pulse welding, severe tempering of martensite occurs present in base metal, resulting in softening

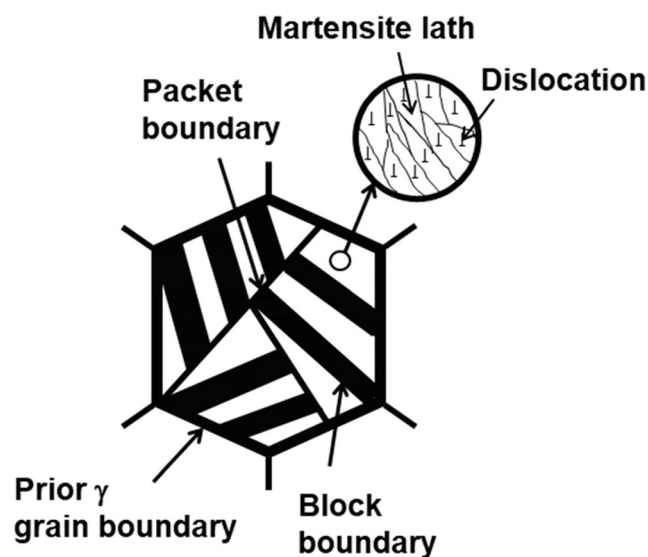


Fig. 24 Schematic illustration showing the substructure of lath martensite [151]

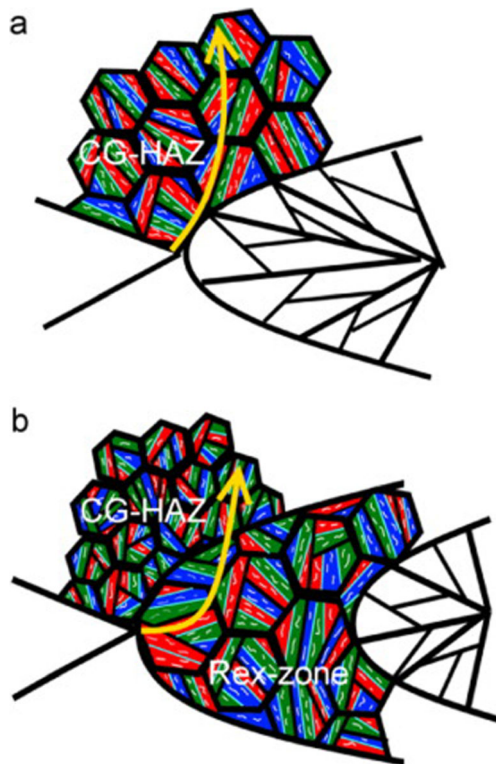


Fig. 25 Schematic illustration of the microstructure and crack path in **a** SPW and **b** DPW [49]

of the SCHAZ which act as failure location at one side of the weld; (ii) formation of coarser structure of Bain groups and low fraction of high angle boundaries along with lower residual strain in REX zone, which effectively restrict the crack propagation as more energy is required for crack to intersect coarser equiaxed PAGs; and (iii) after crossing the Rex zone, the crack path deviates through the CGHAZ which has high fraction of high angle boundaries, fine equiaxed PAGs, fine martensite packets, and Bain groups that retard further crack propagation.

In another study, Chabok et al. [131] examined the effect of lower second pulse current (i.e. 6.4 kA) on residual stresses at weld nugget edge and crystallographic features of the martensite in CGHAZ of SPW and REX zones of DPW of DP1000 steel resistance spot weld. In against to previous finding, they reported that CT peak load and failure energy of DPW decreased compared to SPW. The better mechanical performance of SPW was attributed to the presence of high compressive residual stress perpendicular to the plane of pre-crack compared to REX zone of DPW, which effectively restrain crack tip opening and thus increase the amount of energy required for crack initiation and propagation during CT loading. They reported that during RSW, weld joint experienced the thermal cycle and plastic deformation due to force applied by the electrodes. Residual stresses were buildup because of plastic deformation at the nugget edge. The heat input during in situ PWHT was able to release the residual stresses

in the Rex-zone of the DPW at low second pulse welding current (i.e. 6 kA), leading to low CT peak load and failure energy. However, at higher second pulse current (i.e. 8 kA), DPW experienced higher amount of plastic deformation compared to the SPW. As the plastic deformation increased, compressive residual stresses were built up in front of pre-crack, thus lead to enhanced fracture toughness [131]. In another study, Eftekharimilani et al. [122] reported the ellipticity of the PAGs, defined as $(a - b)/a$ (where a and b are major and minor ellipse radii, respectively), is decreased and equiaxed grains were formed in Rex zone of DPW compared to CGHAZ of SPW, as shown in Figure 26. The higher ellipticity of PAGs in SPW was due to the typical directional solidification of the grains at the weld edge and offers lower resistance to crack propagation compared to equiaxed grains of REX zone. In addition, martensite in REX zone of DPW showed higher Kernel average misorientation (KAM) angle distribution and density of geometrically necessary dislocation compared to the nugget edge of SPW, resulting in improved fracture toughness of the weld joint.

4.4 Effect of in PWHT on elemental distribution and mechanical properties of RSW joint

In RSW, the weld nugget is solidified under non-equilibrium condition due to rapid cooling rates inherent to the process. Compared to the basic composition of the alloy, a change in alloy composition takes place in the crystals being precipitated because of insufficient diffusion occurs during solidification [25]. As a result, alloying elements like manganese, sulphur, and phosphorous present in the steel tend to segregation at PAG boundaries mainly at weld nugget edge and leads to embrittlement of the joint [68, 69]. The elemental segregation in the nugget is also an important factor that affects the mechanical properties and failure mode of the weld. Although crack can generate from the HAZ, the crack path is dictated by the local microstructure and the elemental distribution at the nugget edge [122]. It has been widely reported that applying a second pulse current to RSW joint results in homogenizing of the detrimental elements at the primary weld nugget edge thus leading to improved mechanical properties of the joint. Eftekharimilani et al. [122] determine the effect of in situ PWHT on Phosphorous distribution at nugget edge of 1 GPa complex phase steel resistance spot weld. Based on electron probe microanalysis (EPMA) results, they found that Phosphorous segregation was significantly reduced in annealed zone (refer to Figure 27) compared to traditional SPW. They reported that as the temperature during in situ PWHT increases, the redistribution of Phosphorous in the weld becomes effective. A similar observation has been reported by Van der Aa et al. [133], Koichi et al. [147], and Sawanishi et al. [145] that applying the second pulse current reduces the Phosphorous segregation at nugget edge of

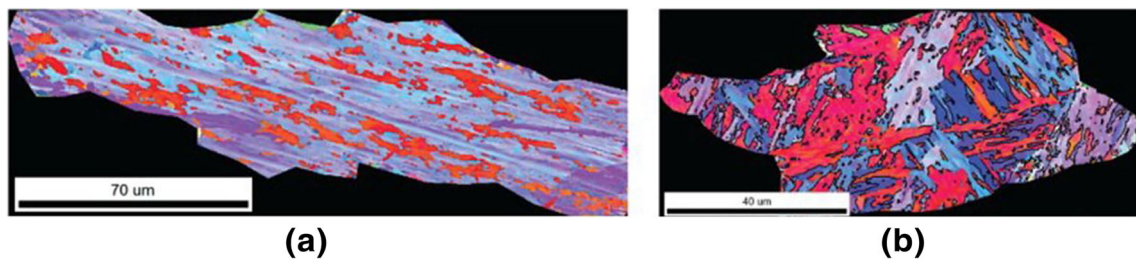
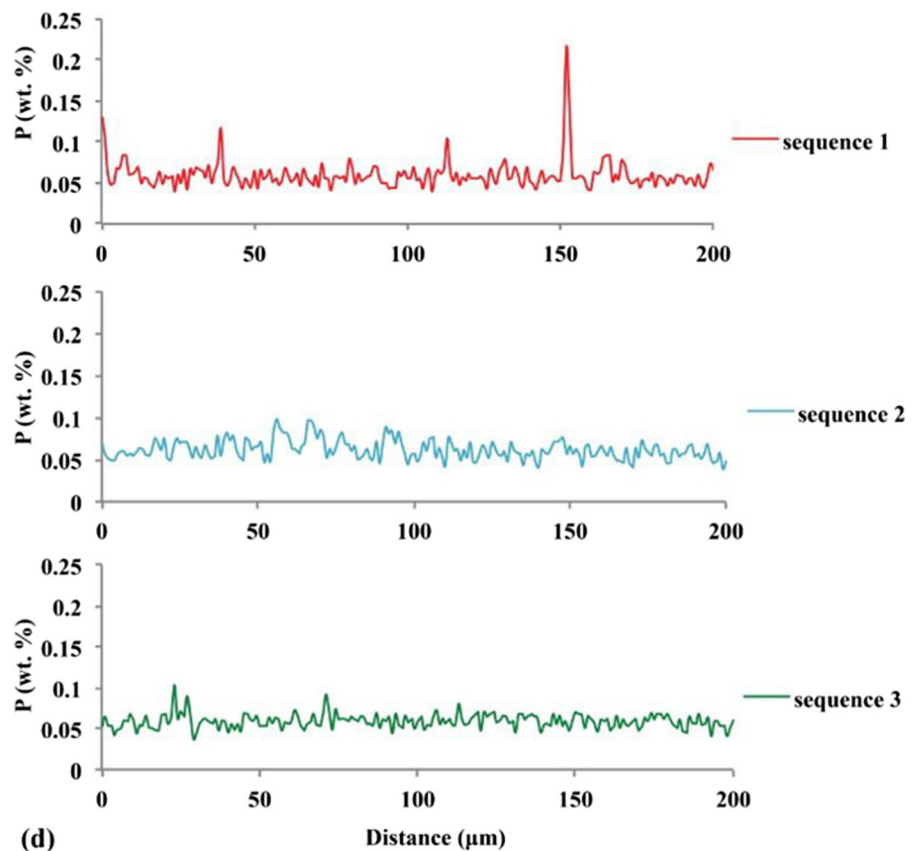
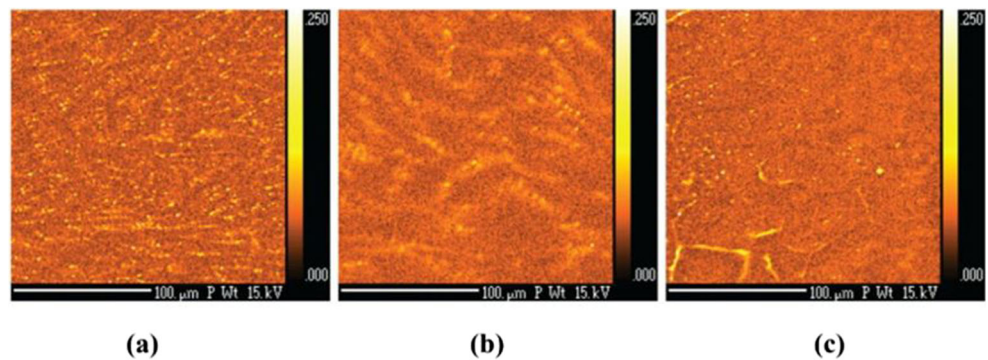


Fig. 26 EBSD micrographs showing IPF map: **a** PAG in SPW and **b** PAG in DPW [122]

automotive steel weld. Wakabayashi et al. [83] found that applying second pulse current reduces the Mn segregation at nugget edge of low carbon steel, thus promoting the PF mode. Medium Mn steels are considered as third generation AHSS

which contain significant amount of Mn in composition to retain austenite at room temperature [153]. However, segregation of Mn in weld nugget during RSW can restrict the wide usage of these steels in automotive applications. Zhao et al.

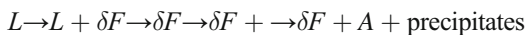
Fig. 27 Compositional maps of showing distribution of P at the annealed zone. Line scans showing P distribution in RSW of 1 GPa complex phase steel RSW at nugget edge; **a** sequence 1 represents SPW, **b** sequence 2 represents DPW treated with second pulse current of 5.7 kA, and **c** sequence 3 represents DPW treated with second pulse current of 6.2 kA [122]



[149] investigated the effect of tempering pulse on Mn distribution of a 7 Mn steel resistance spot weld nugget. EPMA results showed that Mn segregated along the PAG boundaries in conventional weld provided preferred fracture path for crack propagation, as shown in Figure 28a. With the application of postweld pulses (i.e. 4 kA for 20 ms), Mn atoms diffused from the PAG boundaries to the grains attributing to the concentration gradient in nugget, as shown in Figure 28b. They also reported that due to the short postweld time, the separation of Mn along the PAG boundaries cannot be completely eliminated and the weld failed in IF mode.

4.5 Effect of in situ PWHT on austenite-ferrite balance in duplex stainless steel RSWs

The most crucial feature of duplex stainless steel is the ferrite-austenite phase balance in microstructure. During RSW, the FZ of DSS weld follows the solidification path given as



where L is liquid, δF is delta ferrite, and A is austenite. The high cooling rate of the RSW process prevents the nucleation and growth process of the austenite formation, promoting the fully ferritic microstructure accompanied by precipitation of Cr_2N [64, 65]. Arabi et al. [63] showed that the phase balance in FZ of DSS spot weld could be improved using in situ PWHT when the temperature remains below melting point of base metal. Figure 29 shows the microstructure of FZ of DSS resistance spot weld before and after in situ PWHT. They found that the average austenite volume fraction increased from 4 to 30% after applying second pulse current of 5 kA for 1.8 s. The improvement in austenite phase results in enhanced corrosion resistance of FZ. However, effect of austenite phase balance on mechanical properties was not investigated.

4.6 Liquid metal embrittlement control using multi pulse current RSW

LME in automotive steel resistance spot weld can occur via different mechanism and several advantageous thermo-mechanical conditions can increase the susceptibility towards the LME-cracking. Although multiple mechanisms of LME in Zn-coated automotive steel resistance spot weld are reported in literature [24, 154], however, two classical models are generally most widely cited mechanisms for LME crack formation, i.e. (1) liquid Zn penetration model and (2) solid Zn diffusion model [154]. The development stages of LME cracks according liquid zinc penetration model and solid Zn diffusion model are shown in Figure 30. According to liquid Zn penetration model, the LME cracks during RSW of zinc-coated steel are formed by the intrusion of liquid Zn along austenite grain boundaries (GBs). Generally, austenitic microstructures are thought to be more susceptible to LME cracking [24, 155]. As the critical amount of Zn penetration is reached, the steel matrix's ability to support additional stress is compromised. Separation along the Zn penetrated grain boundaries is caused by the stresses exerted by electrodes, resulting in the formation of cracks. [24]. According to Zn diffusion model, Zn atoms diffuse along austenite GBs of the steel as the diffusion rate is very high due to high temperature condition during RSW. After Zn diffusion, austenite GBs transforms to $\alpha\text{-Fe}(\text{Zn})$, as Zn is a strong ferrite stabilizer. Consequently, GBs becomes weak and cracks formed under tensile stresses [154, 156]. LME generally is not acceptable in automotive industry as it can have detrimental effects on weld strength in extreme situations [143]. Although significant amount of work has been conducted to understand the underlying mechanism of LME during RSW of Zn coated steels, however; less focus is given to develop prevention methods. Therefore, it is much needed to explore the new ways to prevent LME cracking in automotive steels. Some methods have been developed to reduce LME cracking, including increasing

Fig. 28 Elemental Maps of Mn **a** without postweld pulse and **b** with postweld pulse [149]

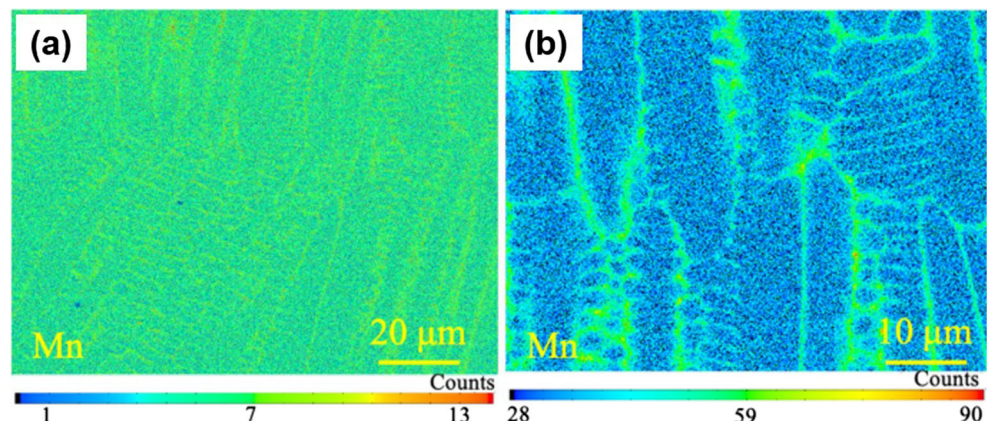
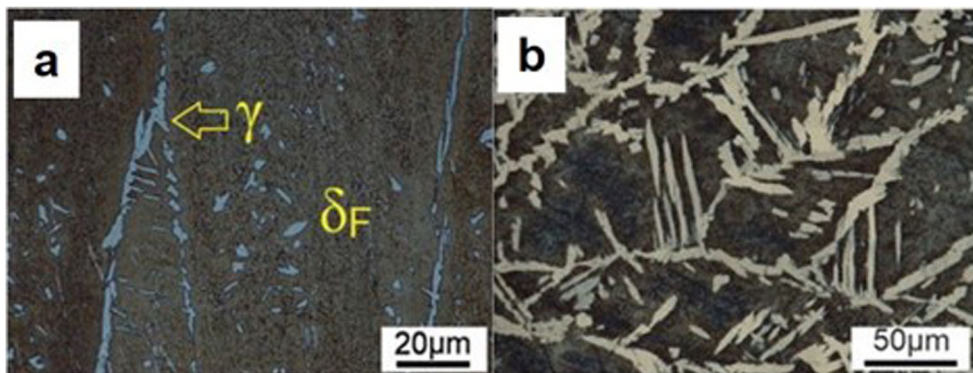


Fig. 29 FZ microstructure of DSS RSW **a** before in situ PWHT and **b** after in situ PWHT at 5 kA for 1.8 s [63]



electrode force or using pulse welding schedule [73, 75, 142, 143, 157]. Pulse welding includes two different approaches (1) multi pulse welding schedule to control heat input at the location of LME cracks and (2) pre-current/pre-pulse welding schedule to remove the zinc coating [143]. Table 4 summarized the outcomes of studies conducted to control LME using different pulse welding schedules.

Ashiri et al. [142] developed impulse welding schedule to mitigate the LME problem in TWIP steel. They used two pulse welding current schedules with 1 cycle of cooling time between first and second pulse. The first pulse was intended to form the minimum nugget size according to $4t^{0.5}$ criterion, and then second pulse was applied with aim to increase weldable current range to enhance the nugget size without causing

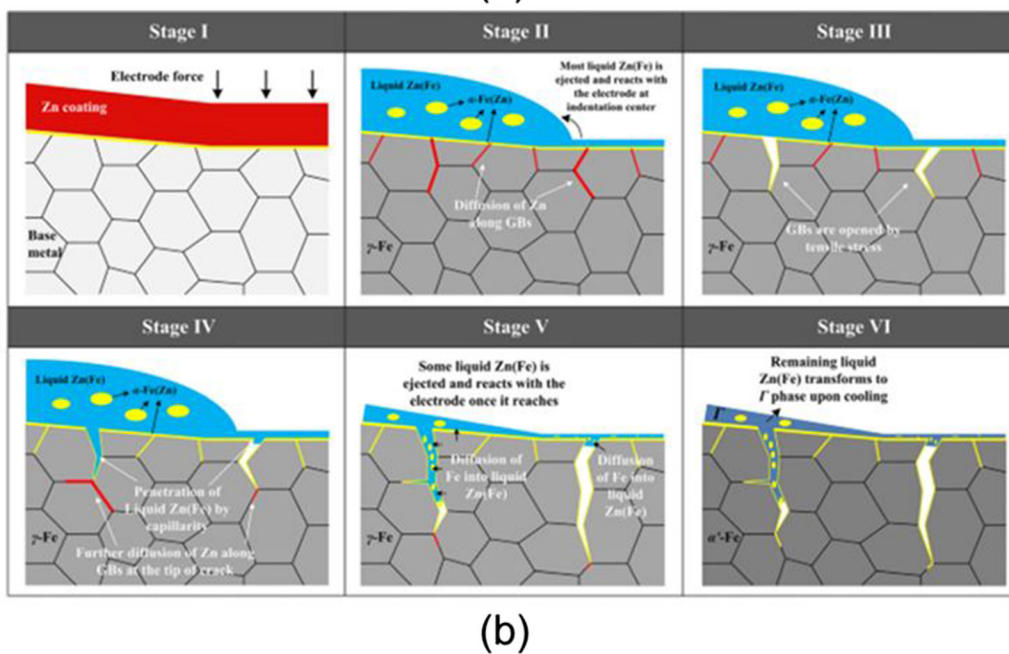
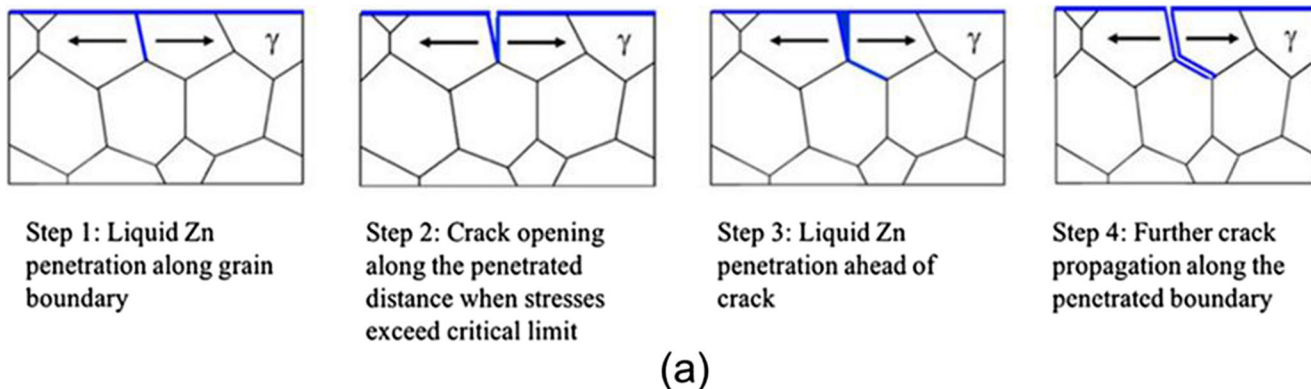


Fig. 30 Mechanism of LME crack formation in steel RSW. **a** Stages of crack formation according to liquid Zn penetration model [24] and **b** stages of crack formation according to Zn solid diffusion model [154]

Table.4 Summary of studies conducted on effect of pulse-RSW on LME of steel resistance spot weld

Base metal(s)/ thickness	Welding schedule	Observation on LME	Ref
Hot-dip galvanized TRIP1100 steel/IF steel 1.6mm /1.5 mm	1. Multi pulse welding schedule 2. Pre-current welding schedule.	1. Reduces the weld surface LME cracks to some extent by stabilizing the Zn coating with Fe alloy and controlling the temperature and stress states in the weld. However, long cracks in centre and small cracks at surface still existed in weld. 2. High heat input schedule increased the LME severity due to the melting of Zn coating. However, low heat input schedule reduced LME by 29%.	[143]
Electrogalvanized TWIP steel Galvannealed TWIP steel Galvanized TWIP steel	Multi pulse welding schedule in which both pulses have similar welding current	Improved the weldability current range without LME	[142]
Galvanized TRIP 1100/1.6 mm	Ramp down current welding schedule	Compared to a constant current, the severity of LME was reduced by 60%.	[158]
Galvannealed TRIP590 steel/1.6 mm	Pre-current welding schedule	Significant reduction in LME at optimum pre-pulse condition	[73]

LME. Three different approaches were used with same primary welding current but different welding times, i.e. (1) long-time second pulse, short-time second pulse, and intermediate-time second pulse. They claimed that short time-second pulse current successfully produces LME free welds due to the slower rate of the nugget growth. Moreover, they found that weldable current range increased by 85.7% compared with similar weldable current range of conventional single-pulse welding schedule. The heat input, was not held constant through the various pulsing conditions, implying that the effect of pulsing cannot be separated from the effect of changing the heat input. Kim et al. [73] showed that applying a pre-pulse reduced the intensity of LME cracks in galvannealed TRIP590 weld. Prior to the application of the main welding pulse, the pre-pulse was designed to melt the liquid zinc, while the electrode forces to squeeze the melt out of the weld region. They claimed that LME reduction occurs as a result of applying a pre-pulse with a lower current than the main welding current leading to removal of the zinc coating, Moreover, two pre-pulse currents were used which can increase the welding time, implying that the method's potential and limitations have yet to be thoroughly explored.

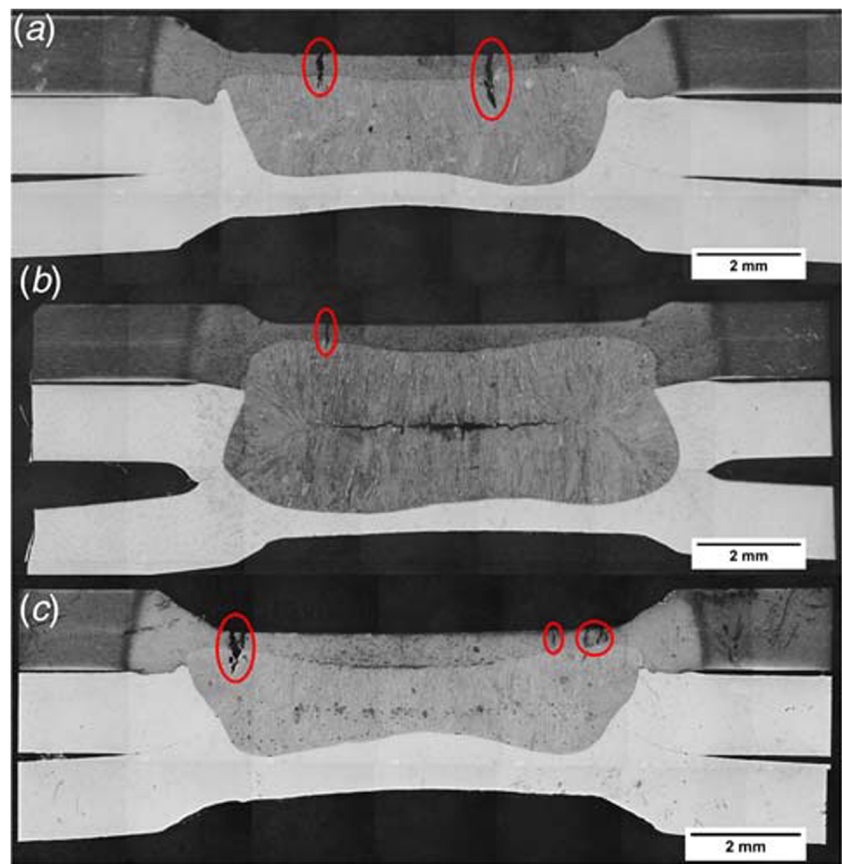
Di Giovanni et al. [158] evaluated the effect of ramp (or linear down slope) welding current schedule on LME cracking of Zn coated TRIP1100 steel resistance spot weld. They showed that ramp down current can mitigate tensile stresses after electrode release, as the indentation weld surface temperature profile spent less time in the liquid zinc region leading to less opportunity for LME cracks to form. However, the study did not offer a satisfactory explanation for the mechanism by which the changes in LME severity are occurred. Wintjes et al. [19] also attempted to reduce LME cracking using

pulse welding schedules during RSW of galvanized TRIP1100 steel. They used three different constant current pulsed welding schedules given as (1) short pulse followed by a long pulse, (2) equal length pulses, and (3) long pulse followed by a short pulse. They found that LME cracks were formed at surface and in centre of the welds in all three types of pulse welding schedules, as shown in Figure 31. The weld made with longer first pulse followed by short pulse exhibited smaller cracks compared with other welds. Reduction in LME cracks was attributed to stabilizing of Zn coating with iron alloying, controlling the temperature and stress states of the weld. However, they failed to explain crack formation in centre of welds. In case of pre-pulse, they used following three schedules were used: (1) high current-long time, (2) high current-short time, and (3) low current-long time. A similar finding was observed for welds subjected to pre-pulse welding schedules, that LME cracks are still visible at both surface and centre of the welds, as shown in Figure 32. However, the weld made with a low current pre-pulse exhibited low LME susceptibility compared to welds made with high pre-pulse current. Reduction in LME cracks was attributed to stabilizing of zinc coating through iron diffusion without melting the coating. Moreover, the findings of the study contradicted with LME mechanisms proposed by Ashiri et al [142] in case of pulse-welding schedules and with Kim et al. [73] in case of pre-pulse welding schedules.

4.7 Critical analysis and future research outlook of pulsed-RSW

1. Although, tempering of martensite is well documented in the literature, but it has been addressed mostly to fully

Fig. 31 Welds made using pulse-RSW schedules: **a** short pulse followed by a long pulse; **b** equal length pulses; **c** long pulse followed by a short pulse [143]

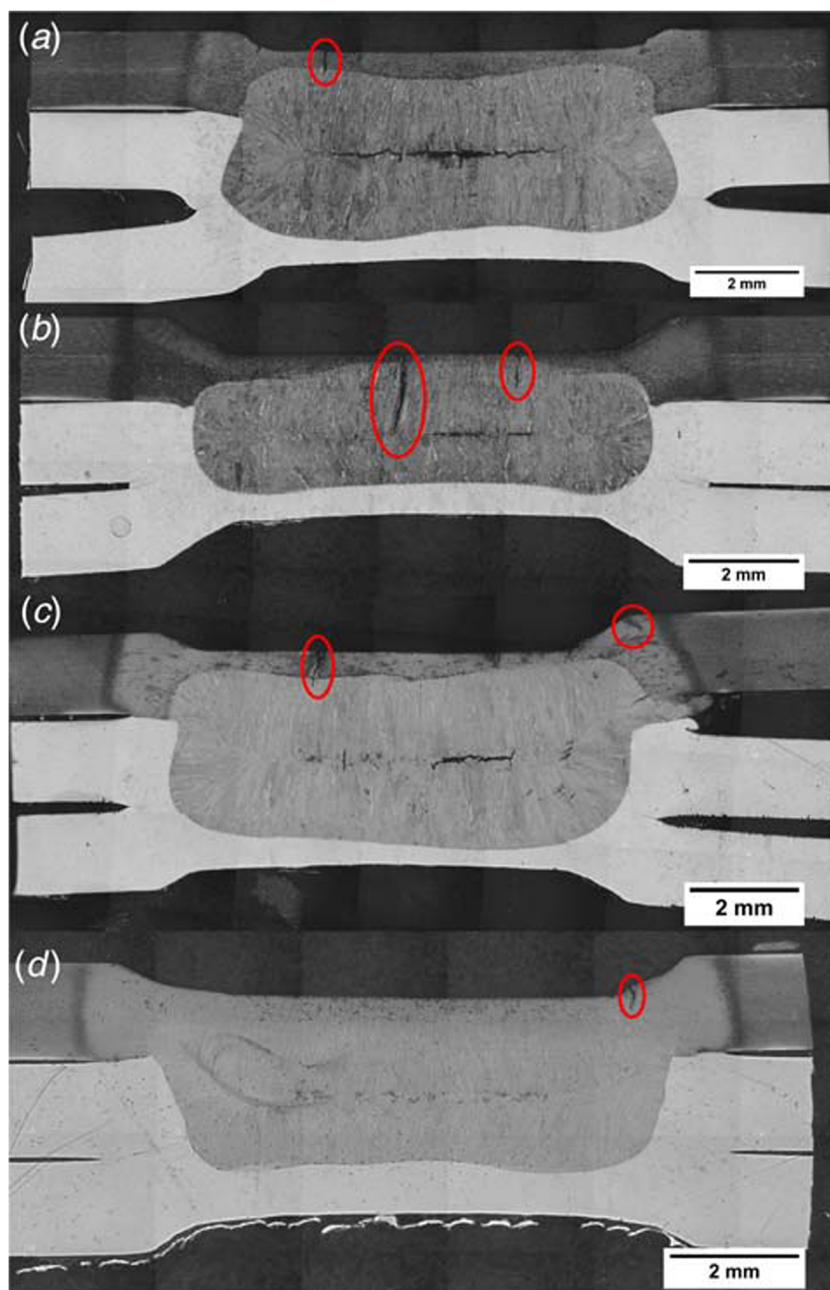


- martensitic steels with equiaxed PAGs subjected to conventional isothermal tempering treatment. The mechanism of tempering of lath martensite formed within large columnar PAGs including carbide nucleation and growth process in FZ of resistance spot weld subjected to non-isothermal tempering during pulsed-RSW is still not clear. Therefore, more research work is needed to understand the various phase transformations which occurs during non-isothermal heating and cooling of AHSS resistance spot welds.
- Experimental temperature measurement during RSW is difficult due to invisible nugget and constricted weld area. Finite element (FE) models need to develop for precise temperature measurement and heat distribution during heating and cooling stage of weld. This would help in deciding the process parameters, i.e. welding current, welding time and holding time which in turn help in controlling tempering temperature.
 - Electrodes with excessively large face diameter provide heat sink to the weld during tempering thus reducing the temper effectiveness. Therefore, electrode diameter with minimum size can be effective for rapid tempering but can also affect the nugget size. Therefore, further studies are required to explore the potential of using smaller electrodes.
 - Fatigue strength of resistance spot weld is equally important as static and impact strength. The microstructural changes imparted during pulse welding can affect fatigue life of the weld. However, no studies have been conducted so far to determine the effect of pulsing on fatigue strength of the weld. Therefore, it is required to conduct further studies to determine the effect of pulsing on fatigue life of automotive steel resistance spot.
 - Although some researchers have successfully reduced LME cracking using pulse-RSW schedules, however, this method is only effective for reducing LME cracks partially. Obtaining LME-free welds is still challenge for automotive manufacturers. This calls for designing more dedicated schedules to eliminated the factors causing LME.

5 Summary

This paper gives an overview of the three modified RSW process, i.e. IA-RSW, MA-RSW, and pulsed-RSW used to improve the weldability and mechanical performance of AHSSs weld while pertaining to their challenges and opportunities.

Figure 32 Welds made using pre-pulse RSW schedules: **a** no pre-pulse; **b** high current-long time. (2) High current-short time. (3) Low current-long time [143]



IA-RSW In this method, a transition material is placed between base metal sheets to modify the chemical composition/microstructure of weld nugget. This mechanism either serves to limit the formation of brittle martensitic structure in FZ via dilution process or to attain metal matrix composite with aim to inhibit the IF mode and to improve the joint mechanical properties. In case of dissimilar alloy, welding interlayers are added at weld interface to form IMCs with improved metallurgical bonding. The criteria for the selection of interlayer depend upon multi factors such as physical properties, metallurgical compatibility, and thickness of the interlayer.

MA-RSW In this method, an externally applied magnetic field interacts with the welding current to produce a Lorentz force which induces EMS in weld pool. The EMS in turn influences the heat and mass transfer during the welding. The externally applied magnetic field can significantly improve the joint mechanical properties of similar AHSS welds. The EMS reduces the temperature gradient in the weld pool during heating stage, and a peanut shell-shaped nugget with increase in diameter is formed. Moreover, during solidification, the inertial movement of the liquid metal in nugget is likely to promote the fragmentation of the dendrites and reduce the shrinkage cavities. Studies have shown that MA-RSW weld exhibit higher load bearing,

and energy absorption capacity and a higher probability of PF mode compare with the traditional RSW weld.

Pulse-RSW In this method, during welding, a second pulse is applied just after the primary welding pulse to temper the martensitic structure or to alter the microstructure of FZ of AHSS weld. Generally, two types of pulsed-RSW schemes are used, i.e. (i) tempering at low current and long pulse time and (ii) tempering at high current and short pulse time. Pulsed-RSW can be used to promote IF to PF mode transition and improved mechanical properties of the weld can be obtained if proper second pulse parameters are used. During pulsed-RSW, temperature is influenced by heat input which in turn depends upon second pulse welding current, second pulse welding time, and cooling time. When peak temperature of weld nugget during second pulse is below Ac1 temperature, martensite tempering occurs leading to improved fracture toughness of the weld joint. When temperature during second pulse is between Ac3 and melting temperature, weld nugget edge experiences re-austenitization due to which large columnar grains transform into equiaxed grains with refined martensite packets. Moreover, elemental segregation can be reduced at nugget edge using pulse-RSW. Thus improved peak load and energy absorption under TS and CT loading. Furthermore, the high cooling rate of the RSW reduces the AVF in DSS weld when subjected to traditional RSW. Applying a second pulse current can significantly improve the AVF in DSS resulting in enhanced corrosion resistance of the FZ. Pulse-RSW have also been shown to reduce LME cracking in AHSSs weld. However, this method is only effective for reducing LME cracks partially and still not applicable in automotive assembly line.

Although the addition of interlayer material between substrate steel sheets can reduce weld brittleness, yet the process itself increase the production cost and time which need to be addressed before industrial implementation. The use of the externally applied magnetic field in RSW process has prompted some advantages such as enlargement of nugget size, destruction of columnar grains of FZ and better mixing of alloying elements in solidified nugget. However, longer welding time required to keep flow of molten metal can increase the wear of electrode tip due to longer contact time with hot liquid metal. In addition, use of electromagnets can be controlled by changing magnetic field. Applying pulse schedule in RSW cycle have great potential to reduce weld brittleness via tempering the martensitic structure and LME cracks. However, the success of in-process tempering depends upon precise control of heat input and temperature distribution which in turn influenced by process parameters such as second pulse current and time, and cooling time between first and second pulse. Smart pulse schedules are needed to develop to fully control the temperature distribution. Moreover, to understand the effect of pulse-RSW on mechanical

performance of the weld under dynamic loading conditions such as high impact crash and cyclic loading needs further research studies.

Funding The authors received financial support from the Universiti Teknologi PETRONAS Malaysia through Graduate Research Assistantship and YUTP grant (015LC0-185).

Data availability The raw/processed data required to reproduce these findings cannot be shared at this time because this being a review article, it was taken from the published literature.

Code availability Not applicable

Declarations

Conflict of interest The authors declare no competing interests.

References

- Hall JN, Fekete JR (2017) Steels for auto bodies: a general overview in Automotive steels design, metallurgy, processing and applications. R. Rana, S. B. Singh (ed), Woodhead Publishing, pp 19-44
- Joost WJ (2012) Reducing vehicle weight and improving U.S. energy efficiency using integrated computational materials engineering. *JOM* 64:1032–1038. <https://doi.org/10.1007/s11837-012-0424-z>
- Lesch C, Kwiaton N, Klose FB (2017) Advanced high strength steels (Ahss) for automotive applications—tailored properties by smart microstructural adjustments. *Steel Res Int* 88(1-21): 1700210. <https://doi.org/10.1002/srin.201700210>
- Mallick PK (2010) Overview in materials, design and manufacturing for lightweight vehicles, Mallick PK (ed) Woodhead Publishing, pp 1-30
- Keeler S, Kimchi M, Mconey PJ (2017) Advanced high strength steels application guidelines version 6.0. World Auto Steel Report.
- Hilditch TB, de Souza T, Hodgson PD (2015) Properties and automotive applications of advanced high-strength steels (ahss) in welding and joining of advanced high strength steels (ahss): Woodhead Publishing, pp 9-28
- Hovorun TP, Berladir KV, Pererva VI, Rudenko SG, Martynov AI (2017) Modern materials for automotive industry. *J Eng Sci* 4(2):f8–f18. [https://doi.org/10.21272/jes.2017.4\(2\).f8](https://doi.org/10.21272/jes.2017.4(2).f8)
- Nanda T, Singh V, Chakraborty A, Sharma S (2016) Third generation of advanced high-strength steels: processing routes and properties. *Proc Inst Mech Eng Part L: J Mater Des Appl* 233: 209–238. <https://doi.org/10.1177/1464420716664198>
- Bhargava M, Chakraborty S, Barnwal VK, Tewari A, Mishra SK (2018) Effect of microstructure evolution during plastic deformation on the formability of Transformation Induced Plasticity and Quenched & Partitioned AHSS. *Mater Des* 152:65–77. <https://doi.org/10.1016/j.matdes.2018.04.068>
- Demeri MY (2013) Dual phase steels in advanced high-strength steels: science, technology, and applications, Demeri MY (ed) ASM International, United States, pp 95-105
- Zhao J, Jiang Z (2018) Thermomechanical processing of advanced high strength steels. *Prog Mater Sci* 94:174–242. <https://doi.org/10.1016/j.pmatsci.2018.01.006>

12. Frómeta D, Lara A, Molas S, Casellas D, Rehr J, Suppan C, Larour P, Calvo J (2019) On the correlation between fracture toughness and crash resistance of advanced high strength steels. *Eng Fract Mech* 205:319–332. <https://doi.org/10.1016/j.engfracmech.2018.10.005>
13. Aydin H, Essadiqi E, Jung I-H, Yue S (2013) Development of 3rd generation AHSS with medium Mn content alloying compositions. *Mater Sci Eng A* 564:501–508. <https://doi.org/10.1016/j.msea.2012.11.113>
14. Horvath CD (2010) Advanced steels for lightweight automotive structures in Materials, design and manufacturing for lightweight vehicles, P. K. Mallick (ed) Woodhead Publishing, pp 35-77
15. Wu X (2011) Advanced high-strength steel tailor welded blanks (AHSS-TWBs) in Tailor welded blanks for advanced manufacturing, B. L. Kinsey and X. Wu (ed). Woodhead Publishing, pp 118-163
16. Bhargava M, Tewari A, Mishra S (2015) Forming limit diagram of advanced high strength steels (AHSS) based on strain-path diagram. *Mater Des* 85:149–155. <https://doi.org/10.1016/j.matdes.2015.06.147>
17. Shome M, Tumuluru M. (2015) Introduction to welding and joining of advanced high-strength steels (AHSS) in welding and joining of advanced high strength steels (AHSS), M. Shome and M. Tumuluru (ed) Woodhead Publishing, Elsevier, UK pp 1-8
18. Shojaee M, Midawi ARH, Barber B, Ghassemi-Armaki H, Worswick M, Biro E (2021) Mechanical properties and failure behavior of resistance spot welded third-generation advanced high strength steels. *J Manuf Process* 65:364–372. <https://doi.org/10.1016/j.jmapro.2021.03.047>
19. Matlock DK, Speer JG (2009) Third generation of AHSS: microstructure design concepts in microstructure and texture in steels. Springer, London, pp 185–205
20. Li S, Yang S, Lu Q, Luo H, Tao W (2018) A novel shim-assisted resistance spot welding process to improve weldability of medium-mn transformation-induced plasticity steel. *Metall Mater Trans B Process Metall Mater Process Sci* 50:1–9. <https://doi.org/10.1007/s11663-018-1463-9>
21. Wan X, Wang Y, Zhang P (2014) Modelling the effect of welding current on resistance spot welding of DP600 steel. *J Mater Process Technol* 214:2723–2729. <https://doi.org/10.1016/j.jmatprotec.2014.06.009>
22. Pouranvari M, Marashi SPH (2013) Critical review of automotive steels spot welding: process, structure and properties. *Sci Technol Weld Join* 18(361-403):20–403. <https://doi.org/10.1179/1362171813y.0000000120>
23. Eshraghi M, Tschopp MA, Asle Zaem M, Felicelli SD (2014) Effect of resistance spot welding parameters on weld pool properties in a DP600 dual-phase steel: a parametric study using thermomechanically-coupled finite element analysis. *Mater Des* 56:387–397. <https://doi.org/10.1016/j.matdes.2013.11.026>
24. Bhattacharya D (2018) Liquid metal embrittlement during resistance spot welding of Zn-coated high-strength steels. *Mater Sci Technol* 34:1809–1829. <https://doi.org/10.1080/02670836.2018.1461595>
25. H. Zhang, Senkara J (2011) Electrothermal processes of welding in resistance welding: fundamentals and applications second ed. CRC Press pp 53-71
26. Kim JW, Murugan SP, Yoo J-H, Ashiri R, Park Y-D (2019) Enhancing nugget size and weldable current range of ultra-high-strength steel using multi-pulse resistance spot welding. *Sci Technol Weld Join* 25:235–242. <https://doi.org/10.1080/13621718.2019.1680483>
27. Messler JRW, Jou M (1996) Review of control systems for resistance spot welding: past and current practices and emerging trends. *Sci Technol Weld Join* 1:1–9. 1996/02/01 1996. <https://doi.org/10.1179/stw.1996.1.1.1>
28. Rao SS, Chhibber R, Arora KS, Shome M (2017) Resistance spot welding of galvanized high strength interstitial free steel. *J Mater Process Technol* 246:252–261. <https://doi.org/10.1016/j.jmatprotec.2017.03.027>
29. Luo Y, Rui W, Xie X, Zhu Y (2016) Study on the nugget growth in single-phase AC resistance spot welding based on the calculation of dynamic resistance. *J Mater Process Technol* 229:492–500. <https://doi.org/10.1016/j.jmatprotec.2015.10.006>
30. Podražaj P, Simončič S (2013) Resistance spot welding control based on the temperature measurement. *Sci Technol Weld Join* 18:551–557. <https://doi.org/10.1179/1362171813Y.0000000131>
31. Vijayan V, Murugan S, Son S-G, Park YD (2019) Shrinkage void formation in resistance spot welds: its effect on advanced high-strength-steel weld strength and failure modes. *J Mater Eng Perform* 28:7514–7526. <https://doi.org/10.1007/s11665-019-04465-6>
32. Zhang H, Hu SJ, Senkara J, Cheng S (2000) A statistical analysis of expulsion limits in resistance spot welding. *J Manuf Sci Eng* 122:501–510
33. Jahandideh AR, Hamed M, Mansourzadeh SA, Rahi A (2013) An experimental study on effects of post-heating parameters on resistance spot welding of SAPH440 steel. *Sci Technol Weld Join* 16: 669–675. <https://doi.org/10.1179/1362171811y.0000000053>
34. Feujofack Kemda BV, Barka N, Jahazi M, Osmani D (2020) Optimization of resistance spot welding process applied to A36 mild steel and hot dipped galvanized steel based on hardness and nugget geometry. *Int J Adv Manuf Technol* 106:2477–2491. <https://doi.org/10.1007/s00170-019-04707-w>
35. Doruk E, Pakdil M, Çam G, Durgun İ, Kumru U (2016) Resistance spot welding applications in automotive industry. *Mühendis ve Makina* 57:48–53 Retrieved from <https://dergipark.org.tr/en/pub/muhendismakina/issue/49071/626131>. Accessed 15 Aug 2021
36. Jaber HL, Pouranvari M, Salim RK, Hashim FA, Marashi SPH (2016) Peak load and energy absorption of DP600 advanced steel resistance spot welds. *Ironmak Steelmak* 44:699–706. <https://doi.org/10.1080/03019233.2016.1229880>
37. Wang W, Zhu Q, Liu C, Wei X (2018) An investigation on the resultant-based failure criterion for resistance spot welding joint in crush test. *Int J Crashworthiness* 24:152–162. <https://doi.org/10.1080/13588265.2017.1421012>
38. Pouranvari M, Sobhani S, Goodarzi F (2018) Resistance spot welding of MS1200 martensitic advanced high strength steel: microstructure-properties relationship. *J Manuf Processes* 31: 867–874. <https://doi.org/10.1016/j.jmapro.2018.01.009>
39. Chao Y (2003) Ultimate strength and failure mechanism of resistance spot weld subjected to tensile, shear, or combined tensile/shear loads. *J Eng Mater Technol-trans Asme* 125:125–132
40. Pouranvari M, Hoveida Marashi SP, Jaber HL (2015) DP780 dual-phase-steel spot welds: critical fusion-zone size ensuring the pull-out failure mode. *Materials in Technol* 49:579–585. <https://doi.org/10.17222/mit.2014.184>
41. Mousavi Anijdan SH, Sabzi M, Ghobeiti-Hasab M, Roshan-Ghiyas A (2018) Optimization of spot welding process parameters in dissimilar joint of dual phase steel DP600 and AISI 304 stainless steel to achieve the highest level of shear-tensile strength. *Mater Sci Eng A* 726:120–125. <https://doi.org/10.1016/j.msea.2018.04.072>
42. Chao YJ, Wang K, Miller KW, Zhu XK (2009) Dynamic separation of resistance spot welded joints: part i-experiments. *Exp Mech* 50:889–900. <https://doi.org/10.1007/s11340-009-9276-z>
43. Marashi P, Pouranvari M, Sanaee SMH, Abedi A, Abootalebi SH, Goodarzi M (2013) Relationship between failure behaviour and weld fusion zone attributes of austenitic stainless steel resistance spot welds. *Mater Sci Technol* 24:1506–1512. <https://doi.org/10.1179/174328408x262418>

44. Nikoosohbat F, Kheirandish S, Goodarzi M, Pouranvari M, Marashi SPH (2013) Microstructure and failure behaviour of resistance spot welded DP980 dual phase steel. *Mater Sci Technol* 26:738–744. <https://doi.org/10.1179/174328409x414995>
45. Pouranvari M (2013) Failure mode transition in similar and dissimilar resistance spot welds of HSLA and low carbon steels. *Can Metall Q* 51:67–74. <https://doi.org/10.1179/1879139511y.0000000020>
46. Khan MI, Kuntz ML, Zhou Y (2013) Effects of weld microstructure on static and impact performance of resistance spot welded joints in advanced high strength steels. *Sci Technol Weld Join* 13:294–304. <https://doi.org/10.1179/174329308x271733>
47. Pouranvari M (2012) Susceptibility to interfacial failure mode in similar and dissimilar resistance spot welds of DP600 dual phase steel and low carbon steel during cross-tension and tensile-shear loading conditions. *Mater Sci Eng A* 546:129–138. <https://doi.org/10.1016/j.msea.2012.03.040>
48. Gould J, Khurana S, Li T (2006) Predictions of microstructures when welding automotive advanced high-strength steels. *Weld J* 85:111S–116S
49. Chabok A, van der Aa E, De Hosson JTM, Pei YT (2017) Mechanical behavior and failure mechanism of resistance spot welded DP1000 dual phase steel. *Mater Des* 124:171–182. <https://doi.org/10.1016/j.matdes.2017.03.070>
50. Mimer M, Svensson LE, Johansson R (2004) Process adjustments to improve fracture behaviour in resistance spot welds of ehss and uhss. *Weld World* 48:14–18. <https://doi.org/10.1007/BF03266421>
51. Soomro IA, Pedapati SR, Awang M (2020) Optimization of postweld tempering pulse parameters for maximum load bearing and failure energy absorption in dual phase (DP590) steel resistance spot welds. *Mater Sci Eng A* 803:140713. <https://doi.org/10.1016/j.msea.2020.140713>
52. Sajjadi-Nikoo S, Pouranvari M, Abedi A, Ghaderi AA (2017) In situ postweld heat treatment of transformation induced plasticity steel resistance spot welds. *Sci Technol Weld Join* 23:71–78. <https://doi.org/10.1080/13621718.2017.1323174>
53. Tamizi M, Pouranvari M, Movahedi M (2021) The role of haz softening on cross-tension mechanical performance of martensitic advanced high strength steel resistance spot welds. *Metall Mater Trans A* 52:655–667. <https://doi.org/10.1007/s11661-020-06104-5>
54. Baltazar Hernandez VH, Nayak SS, Zhou Y (2011) Tempering of martensite in dual-phase steels and its effects on softening behavior. *Metall Mater Trans A* 42:3115–3129. <https://doi.org/10.1007/s11661-011-0739-3>
55. Baltazar Hernandez VH, Panda SK, Kuntz ML, Zhou Y (2010) Nanoindentation and microstructure analysis of resistance spot welded dual phase steel. *Mater Lett* 64(207–210):2010–2210. <https://doi.org/10.1016/j.matlet.2009.10.040>
56. Baltazar Hernandez VH, Panda SK, Okita Y, Zhou NY (2009) A study on heat affected zone softening in resistance spot welded dual phase steel by nanoindentation. *J Mater Sci* 45:1638–1647. <https://doi.org/10.1007/s10853-009-4141-0>
57. Biro E, Vignier S, Kaczynski C, McDermid JR, Lucas E, Embury JD, Zhou YN (2013) Predicting transient softening in the subcritical heat-affected zone of dual-phase and martensitic steel welds. *ISIJ Int* 53:110–118. <https://doi.org/10.2355/isijinternational.53.110>
58. Nayak SS, Biro E, Zhou Y (2012) Resistance spot welding of dual-phase steels: heat affected zone softening and tensile properties. *Trends in Welding Research, Proceedings of the 9th International Conference, Chicago, pp 641–649*
59. Pouranvari M (2011) Effect of resistance spot welding parameters on the HAZ softening of DP980 ferrite-martensite dual phase steel welds. *World Appl Sci J* 15:1454–1458
60. Lu Y, Peer A, Abke T, Kimchi M, Zhang W (2018) Subcritical heat affected zone softening in hot-stamped boron steel during resistance spot welding. *Mater Des* 155:170–184. <https://doi.org/10.1016/j.matdes.2018.05.067>
61. Biro E, McDermid JR, Embury JD, Zhou Y (2010) Softening kinetics in the subcritical heat-affected zone of dual-phase steel welds. *Metall Mater Trans A* 41:2348–2356. <https://doi.org/10.1007/s11661-010-0323-2>
62. Nayak SS, Baltazar Hernandez VH, Zhou Y (2011) Effect of chemistry on nonisothermal tempering and softening of dual-phase steels. *Metall Mater Trans A* 42:3242–3248. <https://doi.org/10.1007/s11661-011-0868-8>
63. Arabi SH, Pouranvari M, Movahedi M (2018) Pathways to improve the austenite–ferrite phase balance during resistance spot welding of duplex stainless steels. *Sci Technol Weld Join* 24:8–15. <https://doi.org/10.1080/13621718.2018.1468949>
64. Arabi S, Pouranvari M, Movahedi M (2017) Eelding metallurgy of duplex stainless steel during resistance spot welding. *Weld J* 96:307S–318S
65. Pouranvari M, Alizadeh-Sh M, Marashi SPH (2015) Welding metallurgy of stainless steels during resistance spot welding Part I: fusion zone. *Sci Technol Weld Join* 20:502–511. <https://doi.org/10.1179/1362171815y.0000000015>
66. Duan R, Luo Z, Li Y, Zhang Y, Liu ZM (2014) Novel postweld heat treatment method for improving mechanical properties of resistance spot weld. *Sci Technol Weld Join* 20(100–105):2014–2105. <https://doi.org/10.1179/1362171814y.0000000262>
67. Chao Y (2003) Failure mode of spot welds: interfacial versus pullout. *Sci Technol Weld Join* 8:133–137
68. Amirthalingam M, van der Aa EM, Kwakernaak C, Hermans MJM, Richardson IM (2015) Elemental segregation during resistance spot welding of boron containing advanced high strength steels. *Weld World* 59:743–755. <https://doi.org/10.1007/s40194-015-0250-3>
69. Eftekharamilani P, van der Aa EM, Hermans MJM, Richardson IM (2017) The microstructural evolution and elemental distribution of a 3rd generation 1 GPa advanced high strength steel during double pulse resistance spot welding. *Weld World* 61:691–701. <https://doi.org/10.1007/s40194-017-0459-4>
70. Joaquin A, Elliott AN, Jiang C (2007) Reducing shrinkage voids in resistance spot welds. *Weld J* 86:24–27
71. Zhao D, Wang Y, Liang D, Zhang P (2017) An investigation into weld defects of spot-welded dual-phase steel. *Int J Adv Manuf Technol* 92:3043–3050. <https://doi.org/10.1007/s00170-017-0398-7>
72. Saha DC, Chang I, Park YD (2014) Heat-affected zone liquation crack on resistance spot welded TWIP steels. *Mater Charact* 93:40–51. <https://doi.org/10.1016/j.matchar.2014.03.016>
73. Kim YG, Kim JJ, Kim JS, Chung YI, Choi DY (2014) Evaluation of surface crack in resistance spot welds of zn-coated steel. *Mater Trans* 55:171–175. <https://doi.org/10.2320/matertrans.M2013244>
74. Ghatei Kalashami A, DiGiovanni C, Razmpoosh MH, Goodwin F, Zhou NY (2020) The effect of silicon content on liquid-metal-embrittlement susceptibility in resistance spot welding of galvanized dual-phase steel. *J Manuf Process* 57:370–379. <https://doi.org/10.1016/j.jmapro.2020.07.008>
75. Wintjes E, DiGiovanni C, He L, Biro E, Zhou NY (2019) Quantifying the link between crack distribution and resistance spot weld strength reduction in liquid metal embrittlement susceptible steels. *Weld World* 63:807–814. <https://doi.org/10.1007/s40194-019-00712-5>
76. He L, DiGiovanni C, Han X, Mehling C, Wintjes E, Biro E, Zhou NY (2019) Suppression of liquid metal embrittlement in resistance spot welding of TRIP steel. *Sci Technol Weld Join* 24:579–586. <https://doi.org/10.1080/13621718.2019.1573011>

77. Ling Z, Wang M, Kong L, Chen K (2020) Towards an explanation of liquid metal embrittlement cracking in resistance spot welding of dissimilar steels. *Mater Des* 195:109055. <https://doi.org/10.1016/j.matdes.2020.109055>
78. Kim JU, Murugan SP, Kim JS, Yook W, Lee CY, Ji C, Jeon JB, Park YD (2021) Liquid metal embrittlement during the resistance spot welding of galvanized steels: synergy of liquid Zn, α -Fe(Zn) and tensile stress. *Sci Technol Weld Join* 26:196–204. <https://doi.org/10.1080/13621718.2021.1880816>
79. DiGiovanni C, Biro E, Zhou NY (2019) Impact of liquid metal embrittlement cracks on resistance spot weld static strength. *Sci Technol Weld Join* 24:218–224. <https://doi.org/10.1080/13621718.2018.1518363>
80. Pouranvari M, Mousavizadeh SM, Marashi SPH, Goodarzi M, Ghorbani M (2011) Influence of fusion zone size and failure mode on mechanical performance of dissimilar resistance spot welds of AISI 1008 low carbon steel and DP600 advanced high strength steel. *Mater Des* 32:1390–1398. <https://doi.org/10.1016/j.matdes.2010.09.010>
81. Pouranvari M, Marashi SPH (2013) Key factors influencing mechanical performance of dual phase steel resistance spot welds. *Sci Technol Weld Join* 15:149–155. <https://doi.org/10.1179/136217109x12590746472535>
82. Tan N, Hong J, Lei M, Jin X, Zheng H, Luo Z (2020) Tensile-shear fracture behaviour of resistance spot-welded hot stamping sheet steel with Al–Si coating. *Sci Technol Weld Join* 25:525–534. <https://doi.org/10.1080/13621718.2020.1751404>
83. Wakabayashi C, Furusako S, Miyazaki Y (2015) Strengthening spot weld joint by autotempering acceleration at heat affected zone. *Sci Technol Weld Join* 20:468–472. <https://doi.org/10.1179/1362171815Y.0000000023>
84. (1997) Recommended practices for test methods for evaluating the resistance spot welding behavior of automotive sheet steel materials. D8.9M, AWS
85. (2017) Method of inspection and acceptance levels for resistance spot welds JIS Z 3140. J. I. Standards, Tokyo
86. (1989) Resistance spot welding DVS 2923, Düsseldorf Germany
87. Sheikhi M, Jaderian S, Mazaheri Y, Pouranvari M (2020) Prediction of the failure mode of automotive steels resistance spot welds. *Sci Technol Weld Join* 25:511–517. <https://doi.org/10.1080/13621718.2020.1747765>
88. Pouranvari M, Marashi SPH, Safanama DS (2011) Failure mode transition in AHSS resistance spot welds. Part II: Experimental investigation and model validation. *Mater Sci Eng A* 528:8344–8352. <https://doi.org/10.1016/j.msea.2011.08.016>
89. Pouranvari M, Marashi SPH (2011) Failure mode transition in AHSS resistance spot welds. Part I. Controlling factors. *Mater Sci Eng A* 528:8337–8343. <https://doi.org/10.1016/j.msea.2011.08.017>
90. Pouranvari M, Marashi SPH (2013) Factors affecting mechanical properties of resistance spot welds. *Mater Sci Technol* 26:1137–1144. <https://doi.org/10.1179/174328409x459301>
91. Pouranvari M (2018) Understanding the factors controlling the interfacial failure strength of advanced high-strength steel resistance spot welds: hardness vs. fracture toughness. *Sci Technol Weld Join* 23:520–526. <https://doi.org/10.1080/13621718.2017.1421303>
92. Aghajani H, Pouranvari M (2018) A pathway to produce strong and tough martensitic stainless steels resistance spot welds. *Sci Technol Weld Join* 24:185–192. <https://doi.org/10.1080/13621718.2018.1483065>
93. Azhari-Saray H, Sarkari-Khorrami M, Nademi-Babahadi A, Kashani-Bozorg SF (2020) Dissimilar resistance spot welding of 6061-T6 aluminum alloy/St-12 carbon steel using a high entropy alloy interlayer. *Internet* 124:106876 ISSN 0966-9795; <https://doi.org/10.1016/j.internet.2020.106876>
94. Pouranvari M (2017) Critical assessment 27: dissimilar resistance spot welding of aluminium/steel: challenges and opportunities. *Mater Sci Technol* 33:1705–1712. <https://doi.org/10.1080/02670836.2017.1334310>
95. Arghavani MR, Movahedi M, Kokabi AH (2016) Role of zinc layer in resistance spot welding of aluminium to steel. *Mater Des* 102:106–114. <https://doi.org/10.1016/j.matdes.2016.04.033>
96. Feng Y, Li Y, Luo Z, Ling Z, Wang Z (2016) Resistance spot welding of Mg to electro-galvanized steel with hot-dip galvanized steel interlayer. *J Mater Process Technol* 236:114–122. <https://doi.org/10.1016/j.jmatprotec.2016.05.015>
97. Oikawa H, Ohmiya S, Yoshimura T, Saitoh T (1999) Resistance spot welding of steel and aluminium sheet using insert metal sheet. *Sci Technol Weld Join* 4:80–88. <https://doi.org/10.1179/136217199101537608>
98. Ren D, Liu L (2014) Interface microstructure and mechanical properties of arc spot welding Mg–steel dissimilar joint with Cu interlayer. *Mater Des* 59:369–376. <https://doi.org/10.1016/j.matdes.2014.03.006>
99. Fang Y, Jiang X, Mo D, Zhu D, Luo Z (2019) A review on dissimilar metals' welding methods and mechanisms with interlayer. *Int J Adv Manuf Technol* 102:2845–2863. <https://doi.org/10.1007/s00170-019-03353-6>
100. Mookam N (2019) Optimization of resistance spot brazing process parameters in AHSS and AISI 304 stainless steel joint using filler metal. *Def Technol* 15:450–456. <https://doi.org/10.1016/j.dt.2019.03.005>
101. Das T, Sahoo B, Kumar P, Paul J (2019) Effect of graphene interlayer on resistance spot welded AISI-1008 steel joints. *Mater Res Expr* 6:0865c3. <https://doi.org/10.1088/2053-1591/ab23d6>
102. Das T, Rawal S, Panda SK, Paul J (2021) Resistance spot-welding of AISI-1008 steel joints with MWCNT coating interlayer. *Mater Manuf Process* 36:448–456. <https://doi.org/10.1080/10426914.2020.1843667>
103. Peterson W (1997) Dilution of weld metal to eliminate interfacial fractures of spot welds in high and ultra-high strength steels, presented at the International Conference. *Advances in Welding Technology*, Columbus
104. Li YB, Li DL, David SA, Lim YC, Feng Z (2016) Microstructures of magnetically assisted dual-phase steel resistance spot welds. *Sci Technol Weld Join* 21:555–563. <https://doi.org/10.1080/13621718.2016.1141493>
105. Li Y (2013) Magnetically assisted resistance spot welding of dual-phase steel. *Weld J* 92:124S–132S
106. Huang M, Zhang Q, Qi L, Deng L, Li Y (2020) Effect of external magnetic field on resistance spot welding of aluminum alloy AA6061-T6. *J Manuf Process* 50:456–466. <https://doi.org/10.1016/j.jmapro.2020.01.005>
107. Li Y, Lin Z, Lai X, Chen G, Zhang K (2010) Induced electromagnetic stirring behavior in a resistance spot weld nugget. *Sci China Technol Sci* 53:1271–1277. <https://doi.org/10.1007/s11431-010-0086-4>
108. Li Y, Luo Z, Bai Y, Ao SS (2013) Investigation of induced magnetic force on liquid nugget during resistance spot welding. *Sci Technol Weld Join* 18:329–336. <https://doi.org/10.1179/1362171813y.0000000110>
109. Li Y, Luo Z, Yan F, Duan R, Yao Q (2014) Effect of external magnetic field on resistance spot welds of aluminum alloy. *Mater Des* 56:1025–1033. <https://doi.org/10.1016/j.matdes.2013.12.005>
110. Li YB, Li DL, Lin ZQ, David SA, Feng Z, Tang W (2013) Review: magnetically assisted resistance spot welding. *Sci Technol Weld Join* 21:59–74. <https://doi.org/10.1179/1362171815y.0000000059>
111. Li YB, Shen Q, Lin ZQ, Hu SJ (2013) Quality improvement in resistance spot weld of advanced high strength steel using external

- magnetic field. *Sci Technol Weld Join* 16:465–469. <https://doi.org/10.1179/1362171811y.0000000002>
112. Li YB, Zhang QX, Qi L, David SA (2018) Improving austenitic stainless steel resistance spot weld quality using external magnetic field. *Sci Technol Weld Join* 23:619–627. <https://doi.org/10.1080/13621718.2018.1443997>
 113. Qi L, Li F, Chen R, Zhang Q, Li Y (2020) Improve resistance spot weld quality of advanced high strength steels using bilateral external magnetic field. *J Manuf Process* 52:270–280. <https://doi.org/10.1016/j.jmappro.2020.02.030>
 114. Qi L, Li F, Zhang Q, Xu Y, Han X, Li Y (2021) Improvement of single-sided resistance spot welding of austenitic stainless steel using radial magnetic field. *J Manuf Sci Eng* 143:031004. <https://doi.org/10.1115/1.4048048>
 115. Shen Q, Li Y, Lin Z, Chen G (2011) Impact of external magnetic field on weld quality of resistance spot welding. *J Manuf Sci Eng* 133:051001. <https://doi.org/10.1115/1.4004794>
 116. Shen Q, Li YB, Lin ZQ, Chen GL (2011) Effect of external constant magnetic field on weld nugget of resistance spot welded dual-phase steel DP590. *IEEE Trans Magn* 47:4116–4119. <https://doi.org/10.1109/tmag.2011.2157316>
 117. Yao Q, Luo Z, Li Y, Yan FY, Duan R (2014) Effect of electro-magnetic stirring on the microstructures and mechanical properties of magnesium alloy resistance spot weld. *Mater Des* 63:200–207. <https://doi.org/10.1016/j.matdes.2014.06.004>
 118. Popov VA (1993) Effect of the magnetic field on the formation of the joint in resistance spot welding. *Weld Int* 7:905–907. <https://doi.org/10.1080/09507119309548515>
 119. Li Y, Lin Z, Hu SJ, Chen G (2008) Magnetohydrodynamic behaviors in a resistance spot weld nugget under different welding currents. *Sci. China Ser E Technol Sci* 51:1507–1515. <https://doi.org/10.1007/s11431-008-0115-8>
 120. Villafuerte J, Kerr H (1990) Electromagnetic stirring and grain refinement in stainless steel GTA welds. *Weld J* 69:1–13
 121. Watanabe Y, Takeda T, Sato H (2006) Effect of magnetic field on weld zone by spot welding in stainless steel. *ISIJ Int* 46:1292–1296. <https://doi.org/10.2355/isijinternational.46.1292>
 122. Eftekharimilani P, van der Aa EM, Hermans MJM, Richardson IM (2017) Microstructural characterisation of double pulse resistance spot welded advanced high strength steel. *Sci Technol Weld Join* 22:545–554. <https://doi.org/10.1080/13621718.2016.1274848>
 123. Liu XD, Xu YB, Misra RDK, Peng F, Wang Y, Du YB (2019) Mechanical properties in double pulse resistance spot welding of Q&P 980 steel. *J Mater Process Technol* 263:186–197. <https://doi.org/10.1016/j.jmatprotec.2018.08.018>
 124. Subramanian A, Senthil PV, Jabaraj DB, Devakumar D (2019) Improving mechanical performance of resistance spot welded joints of AISI 409M steel by double pulse current. *Mater Today: Proc* 16:949–955. <https://doi.org/10.1016/j.matpr.2019.05.181>
 125. Zhong N, Liao X, Wang M, Wu Y, Rong Y (2011) Improvement of microstructures and mechanical properties of resistance spot welded dp600 steel by double pulse technology. *Mater Trans* 52(12):2143–2150. <https://doi.org/10.2320/matertrans.M2011135>
 126. Aghajani H, Pouranvari M (2019) Influence of in situ thermal processing strategies on the weldability of martensitic stainless steel resistance spot welds: effect of second pulse current on the weld microstructure and mechanical properties. *Metall Mater Trans A* 50:5191–5209. <https://doi.org/10.1007/s11661-019-05443-2>
 127. Soomro IA, Pedapati SR (2019) Application of in situ post weld heat treatment using double pulse technology and its effect on microstructure and mechanical performance of resistance spot welded HSLA350 steel. *Int J Adv Manuf Technol* 105:3249–3260. <https://doi.org/10.1007/s00170-019-04569-2>
 128. Soomro IA, Pedapati SR, Awang M (2021) Influence of in situ postweld heat treatment on microstructure and failure behavior of dual-phase steel resistance spot weld. *Int J Adv Manuf Technol* 114:3739–3750. <https://doi.org/10.1007/s00170-021-07134-y>
 129. Lee HT, Chang YC (2020) Effect of double pulse resistance spot welding process on 15B22 hot stamped boron steel. *Metals* 10:1279. <https://doi.org/10.3390/met10101279>
 130. Zhang Y, Fu C, Yi R, Ju J (2020) Optimization of double-pulse process in resistance spot welding of hot stamped steel sheet. *ISIJ Int* 60:1284–1290. <https://doi.org/10.2355/isijinternational>
 131. Chabok A, van der Aa E, Basu I, De Hosson J, Pei Y (2018) Effect of pulse scheme on the microstructural evolution, residual stress state and mechanical performance of resistance spot welded DP1000-GI steel. *Sci Technol Weld Join* 23(8):649–658. <https://doi.org/10.1080/13621718.2018.1452875>
 132. Stadler M, Gruber M, Schnitzer R, Hofer C (2019) Microstructural characterization of a double pulse resistance spot welded 1200 MPa TBF steel. *Weld World* 64:335–343. <https://doi.org/10.1007/s40194-019-00835-9>
 133. E. M. Aa et al. (2015) Improved resistance spot weldability of 3rd generation ahss for automotive applications, in 11th International Seminar on Numerical Analysis of Weldability, Graz, Seggau, Austria, Sept 2015
 134. Soomro IA, Pedapati SR (2020) Effect of multi pulse current treatment on microstructure and microhardness of resistance spot welded dual phase steel DP590. *Mater Werkst* 51:699–705. <https://doi.org/10.1002/mawe.201900239>
 135. Wang B, Hua L, Wang X, Li J (2016) Effects of multi-pulse tempering on resistance spot welding of DP590 steel. *Int J Adv Manuf Technol* 86:2927–2935. <https://doi.org/10.1007/s00170-016-8361-6>
 136. Soomro IA, Pedapati SR, Awang M (2021) Double pulse resistance spot welding of dual phase steel: parametric study on microstructure, failure mode and low dynamic tensile shear properties. *Materials* 14:1–19. <https://doi.org/10.3390/ma14040802>
 137. Hernandez VB, Okita Y, Zhou Y (2012) Second pulse current in resistance spot welded TRIP steel-Effects on the microstructure and mechanical behavior. *Weld J* 91:278–285
 138. Hajjani I, Shamanian M, Atapour M, Ashiri R, Ghassemali E (2019) The assessment of second pulse effects on the microstructure and fracture behavior of the resistance spot welding in advanced ultrahigh-strength steel. *TRIP1100. Iran J Mater Sci Eng* 16:79–88. <https://doi.org/10.22068/ijmse.16.2.79>
 139. Terekhov APIAA (2013) Mechanical properties of resistance spot welded joints in zinc-plated TRIP steel. *Weld Int* 28:324–328. <https://doi.org/10.1080/09507116.2013.796684>
 140. Nikoosohbat F, Kheirandish S, Goodarzi M, Pouranvari M (2015) Effect of tempering on the microstructure and mechanical properties of resistance-spot-welded DP980 dual-phase steel. *Mater Technol* 49:133–138
 141. Pouranvari M, Aghajani H, Ghasemi A (2019) Enhanced mechanical properties of martensitic stainless steels resistance spot welds enabled by in situ rapid tempering. *Sci Technol Weld Join* 25:119–126. <https://doi.org/10.1080/13621718.2019.1641962>
 142. Ashiri R, Shamanian M, Salimijazi HR, Haque MA, Bae JH, Ji CW, Chin KG, Park YD (2016) Liquid metal embrittlement-free welds of Zn-coated twinning induced plasticity steels. *Scr Mater* 114:41–47. <https://doi.org/10.1016/j.scriptamat.2015.11.027>
 143. Wintjes E, DiGiovanni C, He L, Bag S, Goodwin F, Biro E, Zhou Y (2019) Effect of multiple pulse resistance spot welding schedules on liquid metal embrittlement severity. *J Manuf Sci Eng* 141(10):101001. <https://doi.org/10.1115/1.4044099>
 144. Taniguchi K, Matsuda H, Ikeda R, Oi K (2016) Heat distribution in welds by short-time high-current post-heating and its improving effect on cross tension strength: development of resistance spot welding with pulsed current pattern for ultrahigh-strength steel

- sheets. *Weld Int* 30:817–825. <https://doi.org/10.1080/09507116.2016.1142194>
145. Sawanishi C, Ogura T, Taniguchi K, Ikeda R, Oi K, Yasuda K, Hirose A (2013) Mechanical properties and microstructures of resistance spot welded DP980 steel joints using pulsed current pattern. *Sci Technol Weld Join* 19:52–59. <https://doi.org/10.1179/1362171813y.0000000165>
146. Chuko WL, Gould JE (2002) Development of appropriate resistance spot welding practice for transformation-hardened steels. A repeatable and effective methodology for producing a temper diagram for different steels is demonstrated. *Weld J* 81:1S–7S
147. Matsushita M, Taniguchi K, Oi K (2013) Development of next generation resistance spot welding technologies contributing to auto body weight reduction. *JFE Tech Rep* 18:111–117
148. Eftekharmilani P, van der Aa EM, Petrov R, Hermans MJM, Richardson IM (2018) Understanding the effect of a paint bake cycle on the microstructure–mechanical properties relationship of a resistance spot welded advanced high strength steel. *Metall Mater Trans A* 49:6185–6196. <https://doi.org/10.1007/s11661-018-4912-9>
149. Zhao B, Wang Y, Ding K, Wu G, Wei T, Pan H, Gao Y (2021) Enhanced cross-tension property of the resistance spot welded medium-mn steel by in situ microstructure tailoring. *Int J Steel Struct* 21:666–675. <https://doi.org/10.1007/s13296-021-00464-3>
150. Wei ST, Lv D, Liu RD, Lin L, Xu RJ, Guo JY, Wang KQ (2014) Similar and dissimilar resistance spot welding of advanced high strength steels: welding and heat treatment procedures, structure and mechanical properties. *Sci Technol Weld Join* 19(427–435): 2014–2435. <https://doi.org/10.1179/1362171814y.0000000211>
151. Maki T (2012) Morphology and substructure of martensite in steels in *Phase Transformations in Steels*, pp 34–58
152. Hidalgo J, Santofimia MJ (2016) Effect of prior austenite grain size refinement by thermal cycling on the microstructural features of as-quenched lath martensite. *Metall Mater Trans A* 47:5288–5301. <https://doi.org/10.1007/s11661-016-3525-4>
153. Perlade A, Antoni A, Besson R, Caillard D, Callahan M, Emo J, Gourgues AF, Maugis P, Mestrallet A, Thuinet L, Tonizzo Q, Schmitt JH (2019) Development of 3rd generation medium Mn duplex steels for automotive applications. *Mater Sci Technol* 35: 204–219. <https://doi.org/10.1080/02670836.2018.1549303>
154. Ling Z, Chen T, Kong L, Wang M, Pan H, Lei M (2019) Liquid metal embrittlement cracking during resistance spot welding of galvanized Q&P980 Steel. *Metall Mater Trans A* 50:5128–5142. <https://doi.org/10.1007/s11661-019-05388-6>
155. Takahashi M, Nakata M, Imai K, Kojima N, Otsuka N (2017) Liquid metal embrittlement of hot stamped galvanized boron steel sheet-effect of heating time on crack formation. *ISIJ Int* 57: 1094–1101. <https://doi.org/10.2355/isijinternational.ISIJINT-2016-730>
156. Murugan SP, Kim J, Kim J, Wan Y, Lee C, Jeon JB, Park YD (2020) Role of liquid Zn and α -Fe(Zn) on liquid metal embrittlement of medium Mn steel: An ex-situ microstructural analysis of galvanized coating during high temperature tensile test. *Surf Coat Technol* 398:126069. <https://doi.org/10.1016/j.surfcoat.2020.126069>
157. Cheon JY, Vijayan V, Murgun S, Park YD, Kim JH, Yu JY, Ji C (2019) Optimization of pulsed current in resistance spot welding of Zn-coated hot-stamped boron steels. *J Mech Sci Technol* 33: 1615–1621. <https://doi.org/10.1007/s12206-019-0313-2>
158. DiGiovanni C, Bag S, Mehling C, Choi KW, Macwan A, Biro E, Zhou NY (2019) Reduction in liquid metal embrittlement cracking using weld current ramping. *Weld World* 63:1583–1591. <https://doi.org/10.1007/s40194-019-00790-5>

Publisher's note Springer Nature remains neutral with regard to jurisdictional claims in published maps and institutional affiliations.